The Astrophysical Journal Supplement Series, 209:34 (34pp), 2013 December doi:10.1088/0067-0049/209/2/34

THE FIRST FERMI-LAT CATALOG OF SOURCES ABOVE 10 GeV

M. Ackermann[1], M. Ajello[2], A. Allafort[3], W. B. Atwood[4], L. Baldini[5], J. Ballet[6], G. Barbiellini[7,8], D. Bastieri[9,10], K. Bechtol[3], A. Belfiore[4,11,12], R. Bellazzini[13], E. Bernieri[14,15], E. Bissaldi[16], E. D. Bloom[3], E. Bonamente[17,18], T. J. Brandt[19], J. Bregeon[13], M. Brigida[20,21], P. Bruel[22], R. Buehler[1], T. H. Burnett[23], S. Buson[9,10], G. A. Caliandro[3], R. A. Cameron[3], R. Campana[24], P. A. Caraveo[12], J. M. Casandjian[6], E. Cavazzuti[25], C. Cecchi[17,18], E. Charles[3], R. C. G. Chaves[6], A. Chekhtman[26,73], C. C. Cheung[27], J. Chiang[3], G. Chiaro[10], S. Ciprini[25,28], R. Claus[3], J. Cohen-Tanugi[29], L. R. Cominsky[30], J. Conrad[31,32,33,74], S. Cutini[25,28], F. D'Ammando[34], A. de Angelis[35], F. de Palma[20,21], C. D. Dermer[27], R. Desiante[7], S. W. Digel[3], L. Di Venere[20], P. S. Drell[3], A. Drlica-Wagner[36], C. Favuzzi[20,21], S. J. Fegan[22], E. C. Ferrara[19], W. B. Focke[3], P. Fortin[37], A. Franckowiak[3], S. Funk[3], P. Fusco[20,21], F. Gargano[21], D. Gasparrini[25,28], N. Gehrels[19], S. Germani[17,18], N. Giglietto[20,21], P. Giommi[25], F. Giordano[20,21], M. Giroletti[34], G. Godfrey[3], G. A. Gomez-Vargas[38,39,40], I. A. Grenier[6], S. Guiriec[19,75], D. Hadasch[41], Y. Hanabata[42], A. K. Harding[19], M. Hayashida[42], E. Hays[19], J. Hewitt[19], A. B. Hill[3,43,76], D. Horan[22], R. E. Hughes[44], T. Jogler[3], G. Jóhannesson[45], A. S. Johnson[3], T. J. Johnson[46,73], W. N. Johnson[27], T. Kamae[3], J. Kataoka[47], T. Kawano[48], J. Knödlseder[49,50], M. Kuss[13], J. Lande[3], S. Larsson[31,32,51], L. Latronico[52], M. Lemoine-Goumard[53,77], F. Longo[7,8], F. Loparco[20,21], B. Lott[53], M. N. Lovellette[27], P. Lubrano[17,18], E. Massaro[54], M. Mayer[1], M. N. Mazziotta[21], J. E. McEnery[19,55], J. Mehault[53], P. F. Michelson[3], T. Mizuno[56], A. A. Moiseev[55,57], M. E. Monzani[3], A. Morselli[38], I. V. Moskalenko[3], S. Murgia[58], R. Nemmen[19], E. Nuss[29], T. Ohsugi[56], A. Okumura[3,59], M. Orienti[34], J. F. Ormes[60], D. Paneque[3,61], J. S. Perkins[19], M. Pesce-Rollins[13], F. Piron[29], G. Pivato[10], T. A. Porter[3], S. Rainò[20,21], M. Razzano[13,78], A. Reimer[3,41], O. Reimer[3,41], T. Reposeur[53], S. Ritz[4], R. W. Romani[3], M. Roth[23], P. M. Saz Parkinson[4,62], A. Schulz[1], C. Sgrò[13], E. J. Siskind[63], D. A. Smith[53], G. Spandre[13], P. Spinelli[20,21], Łukasz Stawarz[64,65], A. W. Strong[66], D. J. Suson[67], H. Takahashi[48], J. G. Thayer[3], J. B. Thayer[3], D. J. Thompson[19], L. Tibaldo[3], M. Tinivella[13], D. F. Torres[68,69], G. Tosti[17,18], E. Troja[19,55], Y. Uchiyama[70], T. L. Usher[3], J. Vandenbroucke[3], V. Vasileiou[29], G. Vianello[3,71], V. Vitale[38,72], M. Werner[41], B. L. Winer[44], K. S. Wood[27], and M. Wood[3]

[1] Deutsches Elektronen Synchrotron DESY, D-15738 Zeuthen, Germany
[2] Space Sciences Laboratory, 7 Gauss Way, University of California, Berkeley, CA 94720-7450, USA
[3] W. W. Hansen Experimental Physics Laboratory, Kavli Institute for Particle Astrophysics and Cosmology, Department of Physics and SLAC National Accelerator Laboratory, Stanford University, Stanford, CA 94305, USA; digel@stanford.edu
[4] Santa Cruz Institute for Particle Physics, Department of Physics and Department of Astronomy and Astrophysics, University of California at Santa Cruz, Santa Cruz, CA 95064, USA
[5] Università di Pisa and Istituto Nazionale di Fisica Nucleare, Sezione di Pisa, I-56127 Pisa, Italy
[6] Laboratoire AIM, CEA-IRFU/CNRS/Université Paris Diderot, Service d'Astrophysique, CEA Saclay, F-91191 Gif sur Yvette, France
[7] Istituto Nazionale di Fisica Nucleare, Sezione di Trieste, I-34127 Trieste, Italy
[8] Dipartimento di Fisica, Università di Trieste, I-34127 Trieste, Italy
[9] Istituto Nazionale di Fisica Nucleare, Sezione di Padova, I-35131 Padova, Italy
[10] Dipartimento di Fisica e Astronomia "G. Galilei," Università di Padova, I-35131 Padova, Italy
[11] Università degli Studi di Pavia, I-27100 Pavia, Italy
[12] INAF-Istituto di Astrofisica Spaziale e Fisica Cosmica, I-20133 Milano, Italy
[13] Istituto Nazionale di Fisica Nucleare, Sezione di Pisa, I-56127 Pisa, Italy
[14] Istituto Nazionale di Fisica Nucleare, Laboratori Nazionali di Frascati, via E. Fermi 40, I-00044 Frascati (Roma), Italy
[15] Dipartimento di Fisica, Università di Roma Tre, via della Vasca Navale 84, I-00146 Roma, Italy
[16] Istituto Nazionale di Fisica Nucleare, Sezione di Trieste, and Università di Trieste, I-34127 Trieste, Italy
[17] Istituto Nazionale di Fisica Nucleare, Sezione di Perugia, I-06123 Perugia, Italy
[18] Dipartimento di Fisica, Università degli Studi di Perugia, I-06123 Perugia, Italy
[19] NASA Goddard Space Flight Center, Greenbelt, MD 20771, USA
[20] Dipartimento di Fisica "M. Merlin" dell'Università e del Politecnico di Bari, I-70126 Bari, Italy
[21] Istituto Nazionale di Fisica Nucleare, Sezione di Bari, I-70126 Bari, Italy
[22] Laboratoire Leprince-Ringuet, École polytechnique, CNRS/IN2P3, I-91128, Palaiseau, France
[23] Department of Physics, University of Washington, Seattle, WA 98195-1560, USA
[24] INAF-IASF Bologna, I-40129 Bologna, Italy
[25] Agenzia Spaziale Italiana (ASI) Science Data Center, I-00044 Frascati (Roma), Italy
[26] Center for Earth Observing and Space Research, College of Science, George Mason University, Fairfax, VA 22030, USA
[27] Space Science Division, Naval Research Laboratory, Washington, DC 20375-5352, USA
[28] Istituto Nazionale di Astrofisica - Osservatorio Astronomico di Roma, I-00040 Monte Porzio Catone (Roma), Italy
[29] Laboratoire Univers et Particules de Montpellier, Université Montpellier 2, CNRS/IN2P3, F-34095 Montpellier, France
[30] Department of Physics and Astronomy, Sonoma State University, Rohnert Park, CA 94928-3609, USA
[31] Department of Physics, Stockholm University, AlbaNova, SE-106 91 Stockholm, Sweden
[32] The Oskar Klein Centre for Cosmoparticle Physics, AlbaNova, SE-106 91 Stockholm, Sweden
[33] The Royal Swedish Academy of Sciences, Box 50005, SE-104 05 Stockholm, Sweden
[34] INAF Istituto di Radioastronomia, I-40129 Bologna, Italy
[35] Dipartimento di Fisica, Università di Udine and Istituto Nazionale di Fisica Nucleare, Sezione di Trieste, Gruppo Collegato di Udine, I-33100 Udine, Italy
[36] Fermilab, Batavia, IL 60510, USA
[37] Harvard-Smithsonian Center for Astrophysics, Cambridge, MA 02138, USA; fortin@veritas.sao.arizona.edu
[38] Istituto Nazionale di Fisica Nucleare, Sezione di Roma "Tor Vergata," I-00133 Roma, Italy
[39] Departamento de Física Teórica, Universidad Autónoma de Madrid, Cantoblanco, E-28049 Madrid, Spain
[40] Instituto de Física Teórica IFT-UAM/CSIC, Universidad Autónoma de Madrid, Cantoblanco, E-28049 Madrid, Spain
[41] Institut für Astro- und Teilchenphysik and Institut für Theoretische Physik, Leopold-Franzens-Universität Innsbruck, A-6020 Innsbruck, Austria

[42] Institute for Cosmic-Ray Research, University of Tokyo, 5-1-5 Kashiwanoha, Kashiwa, Chiba 277-8582, Japan
[43] School of Physics and Astronomy, University of Southampton, Highfield, Southampton SO17 1BJ, UK
[44] Department of Physics, Center for Cosmology and Astro-Particle Physics, The Ohio State University, Columbus, OH 43210, USA
[45] Science Institute, University of Iceland, IS-107 Reykjavik, Iceland
[46] National Research Council Research Associate, National Academy of Sciences, Washington, DC 20001, USA
[47] Research Institute for Science and Engineering, Waseda University, 3-4-1, Okubo, Shinjuku, Tokyo 169-8555, Japan
[48] Department of Physical Sciences, Hiroshima University, Higashi-Hiroshima, Hiroshima 739-8526, Japan
[49] CNRS, IRAP, F-31028 Toulouse cedex 4, France
[50] GAHEC, Université de Toulouse, UPS-OMP, IRAP, F-31028 Toulouse, France
[51] Department of Astronomy, Stockholm University, SE-106 91 Stockholm, Sweden
[52] Istituto Nazionale di Fisica Nucleare, Sezione di Torino, I-10125 Torino, Italy
[53] Centre d'Études Nucléaires de Bordeaux Gradignan, IN2P3/CNRS, Université Bordeaux 1, BP120, F-33175 Gradignan Cedex, France
[54] Physics Department, Università di Roma "La Sapienza," I-00185 Roma, Italy
[55] Department of Physics and Department of Astronomy, University of Maryland, College Park, MD 20742, USA
[56] Hiroshima Astrophysical Science Center, Hiroshima University, Higashi-Hiroshima, Hiroshima 739-8526, Japan
[57] Center for Research and Exploration in Space Science and Technology (CRESST) and NASA Goddard Space Flight Center, Greenbelt, MD 20771, USA
[58] Center for Cosmology, Physics and Astronomy Department, University of California, Irvine, CA 92697-2575, USA
[59] Solar-Terrestrial Environment Laboratory, Nagoya University, Nagoya 464-8601, Japan
[60] Department of Physics and Astronomy, University of Denver, Denver, CO 80208, USA
[61] Max-Planck-Institut für Physik, D-80805 München, Germany; dpaneque@mppmu.mpg.de
[62] Department of Physics, The University of Hong Kong, Pokfulam Road, Hong Kong, China
[63] NYCB Real-Time Computing Inc., Lattingtown, NY 11560-1025, USA
[64] Institute of Space and Astronautical Science, JAXA, 3-1-1 Yoshinodai, Chuo-ku, Sagamihara, Kanagawa 252-5210, Japan
[65] Astronomical Observatory, Jagiellonian University, 30-244 Kraków, Poland
[66] Max-Planck Institut für extraterrestrische Physik, D-85748 Garching, Germany
[67] Department of Chemistry and Physics, Purdue University Calumet, Hammond, IN 46323-2094, USA
[68] Institut de Ciències de l'Espai (IEEE-CSIC), Campus UAB, E-08193 Barcelona, Spain
[69] Institució Catalana de Recerca i Estudis Avançats (ICREA), E-08010 Barcelona, Spain
[70] 3-34-1 Nishi-Ikehukuro, Toshima-ku, Tokyo 171-8501, Japan
[71] Consorzio Interuniversitario per la Fisica Spaziale (CIFS), I-10133 Torino, Italy
[72] Dipartimento di Fisica, Università di Roma "Tor Vergata," I-00133 Roma, Italy
Received 2013 June 27; accepted 2013 October 14; published 2013 November 14

ABSTRACT

We present a catalog of γ-ray sources at energies above 10 GeV based on data from the Large Area Telescope (LAT) accumulated during the first 3 yr of the Fermi Gamma-ray Space Telescope mission. The first Fermi-LAT catalog of > 10 GeV sources (1FHL) has 514 sources. For each source we present location, spectrum, a measure of variability, and associations with cataloged sources at other wavelengths. We found that 449 (87%) could be associated with known sources, of which 393 (76% of the 1FHL sources) are active galactic nuclei. Of the 27 sources associated with known pulsars, we find 20 (12) to have significant pulsations in the range > 10 GeV (> 25 GeV). In this work we also report that, at energies above 10 GeV, unresolved sources account for 27% ± 8% of the isotropic γ-ray background, while the unresolved Galactic population contributes only at the few percent level to the Galactic diffuse background. We also highlight the subset of the 1FHL sources that are best candidates for detection at energies above 50 100 GeV with current and future ground-based γ-ray observatories.

Key words: catalogs – gamma rays: general

Online-only material: color figures, machine-readable tables, extended figure, supplemental data (FITS) file

1. INTRODUCTION

The primary catalog of γ-ray sources detected by the Fermi Large Area Telescope (LAT), the second LAT source catalog (hereafter 2FGL; Nolan et al. 2012), presents sources detected at energies above 100 MeV in the first 2 yr of science operations. Motivations for studying the γ-ray sky at even higher energies in LAT data are numerous, including finding the hardest-spectrum sources and characterizing them separately from their generally much brighter emission at lower energies. Here we present a catalog of sources detected above 10 GeV in the LAT data.

This work is not the first systematic study of γ-ray sources in the GeV range. Lamb & Macomb (1997) presented a catalog of 57 sources detected above 1 GeV in 4.5 yr of data from the Energetic Gamma-Ray Experiment Telescope (EGRET) on the Compton Gamma Ray Observatory. Relative to the third EGRET catalog of sources detected above 100 MeV (hereafter 3EG; Hartman et al. 1999) the localization regions are smaller and the fraction of sources for which no counterpart at other wavelengths could be confidently assigned is also smaller (53% versus 63% of the 271 3EG sources). Individual sources could not be detected at higher energies with EGRET but Thompson et al. (2005) studied the distribution of the 1506 EGRET γ-rays above 10 GeV and found 187 to be within 1° of a 3EG source. Neronov & Semikoz (2010) searched for sources at energies above 100 GeV in ~2 yr of LAT data for Galactic latitudes |b| < 10°, reporting 19 sources. Neronov et al. (2011) reported strong correlations between > 100 GeV LAT γ-rays and cataloged γ-ray sources.

The current LAT data allow a much deeper exploration of the sky above 10 GeV than has been possible before, with an

[73] Currently at Naval Research Laboratory, Washington, DC 20375, USA.
[74] Royal Swedish Academy of Sciences Research Fellow, funded by a grant from the K. A. Wallenberg Foundation.
[75] NASA Postdoctoral Program Fellow, USA.
[76] Funded by a Marie Curie IOF, FP7/2007-2013 - Grant agreement no. 275861.
[77] Funded by contract ERC-StG-259391 from the European Community.
[78] Funded by contract FIRB-2012-RBFR12PM1F from the Italian Ministry of Education, University and Research (MIUR).

energy range that approaches the > 100 GeV (hereafter VHE) domain studied by imaging atmospheric Cherenkov telescopes (IACTs). Broadband studies of γ-ray sources provide insights into the acceleration and radiation mechanisms operating at the highest energies. The relatively small fields of view and limited duty cycles of IACTs, and the low fluxes of VHE sources, makes target selection very important for source searches with IACTs. According to the TeVCat catalog[79] version 3.400, 105 sources have been detected at VHE,[80] which is approximately 20 times fewer than in the 2FGL catalog. A catalog of > 10 GeV Fermi LAT detections may increase the efficiency of these searches with current generation of IACTs, namely H.E.S.S., MAGIC and VERITAS.

In our catalog of LAT sources above 10 GeV we report the locations, spectra, and variability properties of the 514 sources significantly detected in this range during the first 3 yr of the Fermi mission. Many of these sources are already included in the 2FGL catalog, although in that catalog their characterization is dominated by the much larger numbers of γ rays detected in the energy range 100 MeV–10 GeV. Consequently, the characteristics of the sources at the highest Fermi LAT energies might be overlooked. In addition, several of the sources reported here were not listed in the 2FGL, possibly due to the 33% less exposure. We also develop a set of criteria to select the sources that are the best candidates for detection at VHE with the current generation of IACTs.

In Section 2 we describe the capabilities of the Fermi LAT to perform astronomy at energies above 10 GeV. Section 3 describes the overall Fermi sky above 10 GeV, the analysis procedures, the sources detected and the corresponding associations to known objects. In Section 4 we report on the overall characteristics of these sources, with special focus on active galactic nuclei (AGNs), which constitute the majority of the catalog. Section 5 presents the criteria for selecting sources that may be detectable with the current generation of IACTs operating above 100 GeV. In Section 6 we report on the properties of the source populations above 10 GeV, and in Section 7 we summarize and conclude this work.

2. INSTRUMENT AND BACKGROUND

The Fermi LAT is a γ-ray telescope operating from 20 MeV to > 300 GeV. The instrument is a 4 × 4 array of identical towers, each one consisting of a tracker (where the photons have a high probability of converting to pairs, which are tracked to allow reconstruction of the γ-ray direction) and a segmented calorimeter (where the electromagnetic shower produces scintillation light, from which the γ-ray energy can be estimated). The tracker is covered with an anti-coincidence detector to reject the charged-particle background. Further details on the LAT, its performance, and calibration are given by Atwood et al. (2009) and Ackermann et al. (2012b). In the following subsections we report on the event classification, the corresponding instrument response functions, the data selection, the exposure, and the resulting point-source sensitivity. The sensitivity is derived using the approach presented by Abdo et al. (2010e) for the first Fermi LAT source catalog, which is based on a standard likelihood function formalism. The likelihood combines the data with a model of the sky that includes localized γ-ray sources and diffuse backgrounds and accounts for the instrument response functions and the exposure.

2.1. LAT Event Class Selection

The γ-ray event selection used for this study benefited from the experience acquired by the Fermi LAT collaboration during the first years of operation, which led to the development of the Pass 7 event classifications (Ackermann et al. 2012b). The P7CLEAN event class was used in constructing this catalog as it provides a substantial reduction in residual cosmic-ray background (cosmic rays misclassified as γ-rays) above 10 GeV relative to the P7SOURCE event class used for 2FGL. The isotropic background, which comprises both the diffuse γ-ray and residual cosmic-ray backgrounds, is a factor of approximately five less than for the P7SOURCE event class, which was used for the 2FGL catalog analysis, for which the larger effective area at lower energies was the overriding consideration. The decrease in the isotropic background is dominated by the large reduction in residual charged cosmic rays in the P7CLEAN class, approximately a factor of four at 10 GeV and more than an order of magnitude at 100 GeV, as reported in Ackermann et al. (2012b). For the analyses we used the corresponding P7CLEAN_V6 instrument response functions. The systematic uncertainty in the effective area above 10 GeV is estimated to be 10% (Ackermann et al. 2012b).[81]

2.2. Performance of the LAT

The Fermi LAT has a field of view of ~2.4 sr, and is most sensitive (in E^2dN/dE) for photon energies of about 3 GeV. Above this energy, up to ~300 GeV, the on-axis effective area for P7CLEAN_V6 is at least 0.7 m^2. It rolls off to ~0.65 m^2 by 500 GeV. At γ-ray energies below 10 GeV, the point-spread function (PSF) is dominated by multiple Coulomb scattering in the tracker (which varies inversely with the electron energy). Above 10 GeV the geometry of the tracker itself is the dominant factor, and so the PSF is not as strongly energy dependent as at lower energies. The 68% containment radius of the PSF (Front and Back averaged) is ~0.3 at 10 GeV, narrowing to ~0.2 above 100 GeV. The energy resolution ranges from 8% (68% containment) at 10 GeV to approximately 15% at 500 GeV due to the lack of containment of the electromagnetic shower inside the calorimeter. This does not appreciably affect the sensitivity, because the angular resolution and effective area depend only weakly on energy in this range.

2.3. Data Selection and the Sky above 10 GeV

In this work we analyze γ rays with energies in the range 10–500 GeV. To limit the contamination from γ rays produced by cosmic-ray interactions in the upper atmosphere, γ rays with zenith angles greater than 105° were excluded. To further reduce the residual γ rays from the upper atmosphere only data for time periods when the spacecraft rocking angle was less than 52° were considered. Time intervals with larger rocking angles are typically no more than tens of minutes long, occurring during orbits when the spacecraft was executing pointed observations instead of the standard sky-scanning survey mode. The longest contiguous time interval with rocking angle greater than 52° during the 3 yr considered here (Section 2.4) was 5 hr, during a pointed observation near the orbital pole.

Figure 1 shows the distribution of γ rays above 10 GeV. Since the exposure is quite uniform (Section 2.4), this distribution reflects the spatial variations in the brightness of the sky. The bright band along the Galactic equator is primarily due to diffuse

[79] http://tevcat.uchicago.edu/

[80] Including recently announced VHE detections the number is 143.

[81] See also http://fermi.gsfc.nasa.gov/ssc/data/analysis/LAT_caveats.html.

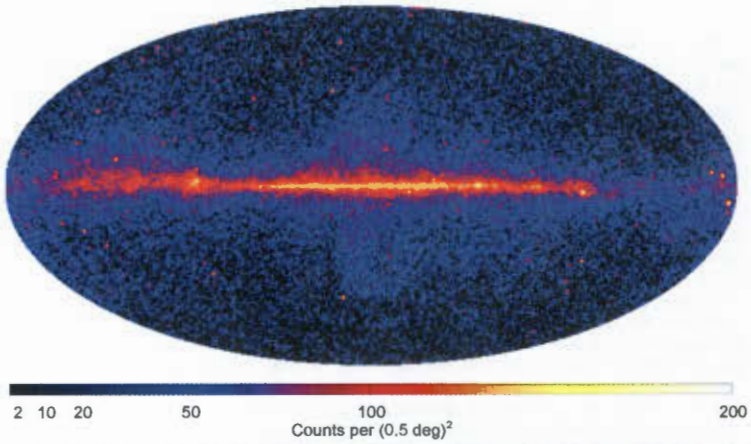

Figure 1. Sky map of γ-ray counts above 10 GeV in Galactic coordinates in Hammer–Aitoff projection. The Galactic center (0,0) is at the center of the map and Galactic longitude increases to the left. The binning is 0.°5 and the image has been smoothed with a two-dimensional Gaussian of full width at half maximum 0.°75. (A color version of this figure is available in the online journal.)

γ-ray emission from cosmic-ray interactions with interstellar gas and radiation. The isotropic background (extragalactic diffuse γ rays and residual local contamination) becomes relatively more important at high latitudes, although structure in the Galactic diffuse emission is still evident, notably in the so-called Fermi bubbles, lobes of hard-spectrum emission above and below the Galactic center (Su et al. 2010). Point sources of γ rays are evident throughout the sky, with some concentration toward the Galactic equator.

At energies above 10 GeV the improved source-background contrast (with respect to the 100 MeV–10 GeV range) provides two benefits: (1) the overall intensity of the diffuse background (Galactic diffuse plus isotropic extragalactic and residual cosmic rays) falls approximately according to a power law of index ~2.4 while the majority of the sources detectable above 10 GeV have harder spectra (many of them with an index smaller than 2.0); (2) the PSF is narrowest at energies above 10 GeV (Section 2.2), and hence the photon signal from a γ-ray source is concentrated in a smaller region. Therefore, above 10 GeV sources can be detected with only 4–5 γ rays (Section 3.2) and the analysis is less affected by the uncertainties and/or inaccuracies in the model for the diffuse backgrounds.

2.4. Exposure, Diffuse Gamma-Ray Backgrounds, and Point-source Sensitivity

The time interval analyzed here is from the beginning of science operations, 2008 August 4 (MET 239557447) to 2011 August 1 (MET 333849586), covering very nearly 3 yr.[82] The overall exposure for the 3 yr interval is relatively uniform (Figure 2), ranging from −15% to +38% of the average value of 9.5×10^{10} cm^2 s, primarily as a function of declination. The exposure at southern declinations is somewhat less because no observations are made during passages through the South Atlantic Anomaly. In addition, the exposure near the northern celestial pole is enhanced because the majority of non-survey mode (pointed) observations have been made toward northern targets. The exposure is slightly depressed in a ~21° diameter region near the southern celestial pole because of the 105° limit on zenith angle for the γ rays selected for analysis (Section 2.3).

Proper quantification of the diffuse backgrounds is necessary for accurate source detection and characterization. We used the publicly available models for the Galactic and isotropic diffuse emissions for this analysis. These files, `gal_2yearp7v6_v0.fits` and `iso_p7v6clean.txt`, can be retrieved from the Fermi Science Support Center[83] (FSSC). The same models were also used in producing the 2FGL catalog.

The sensitivity of the LAT observations depends on the exposure, the diffuse backgrounds, and the PSF. The derived point-source flux sensitivity of the LAT for the 3 yr interval is depicted in Figure 3 for two energy ranges, 10–500 GeV and 100–500 GeV. As for lower energies (see, e.g., Ackermann et al. 2012b), these plots show that the sensitivity ranges by only a factor of two over most of the sky, apart from the inner region of the Galactic plane, where the intense diffuse γ-ray background greatly reduces the point-source sensitivity. The extended, lobe-like features of decreased sensitivity are due to the Fermi bubbles (Section 2.3). The specific shape in Figure 3 is determined by the template for the bubbles in the model for diffuse interstellar γ-ray emission used to evaluate the flux limits.[84] The detection flux-threshold depends very little on the spectral shape outside the Galactic plane (Figure 4). We note that for energies above 100 GeV, the 3 yr point-source sensitivity of the LAT, which is in the range $(2–4) \times 10^{-11}$ photons cm^{-2} s^{-1} for most of the sky, corresponds to about 6 hr of effective observing time for modern IACTs.

3. ANALYSIS AND ASSOCIATION METHODOLOGY

The analysis follows broadly the same steps as the 2FGL catalog (Nolan et al. 2012). The significance of sources is measured by the test statistic $TS = 2\Delta \log L$, comparing the likelihood with and without the source in the model. Source

[82] Mission Elapsed Time (MET), the number of seconds since 00:00 UTC on 2001 January 1 (excluding leap seconds).

[83] See http://fermi.gsfc.nasa.gov/ssc/data/access/lat/BackgroundModels.html.

[84] See http://fermi.gsfc.nasa.gov/ssc/data/access/lat/Model_details/Pass7_galactic.html.

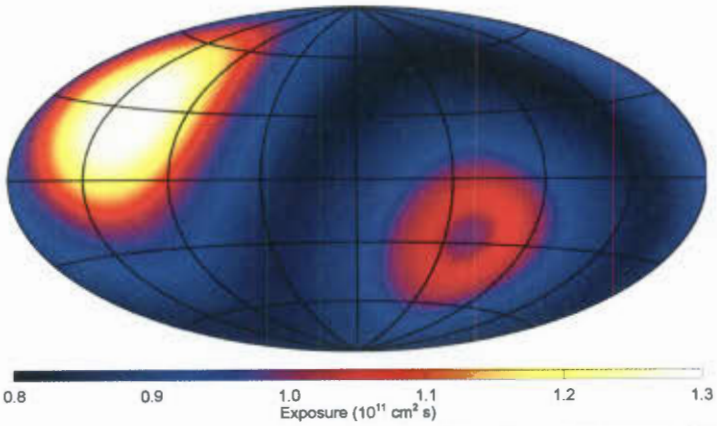

Figure 2. Overall exposure at 10 GeV for the 3 yr time period considered here, in Galactic coordinates in Hammer–Aitoff projection. The same cuts on rocking angle and zenith angle as described in Section 2.3 have been applied. The overall average is 9.5×10^{10} cm^2 s.

(A color version of this figure is available in the online journal.)

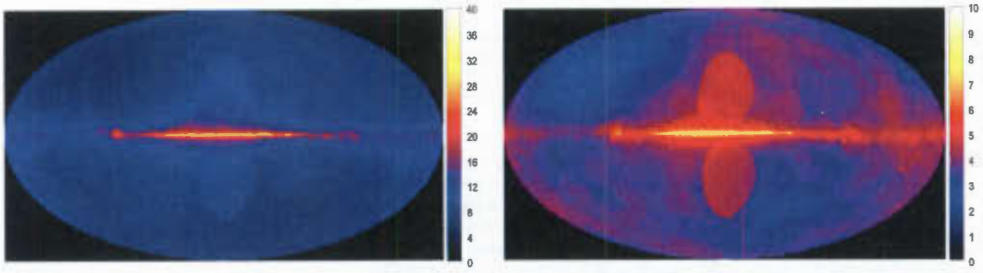

Figure 3. Minimum detectable photon flux (in 10^{-11} photons cm^{-2} s^{-1}) for a γ-ray point source (with spectral index of 2.5) after 3 yr for 10–500 GeV (left) and for 100–500 GeV (right). The images are in Hammer–Aitoff projection in Galactic coordinates. The images are available as FITS files in the electronic edition and from the FSSC.

(A color version and supplemental data for this figure are available in the online journal.)

detection and characterization began with the assembly of a list of "seeds" (Section 3.1), candidate sources that were selected for input to the likelihood analysis chain. The seeds were supplied to the standard maximum likelihood analysis that was used to jointly optimize the spectral parameters of the candidate sources and to judge their overall significances (Section 3.2). The search for source variability differs from the 2FGL analysis owing to the limited statistics of the data (Section 3.3). In the final step of the analysis we searched for candidate counterparts of these 1FHL sources with sources in previous LAT catalogs and sources in known γ-ray-emitting classes at other wavelengths (Section 3.4).

3.1. Seed Selection and Localization

The list of seeds and their locations were obtained in the same way as for the 2FGL catalog analysis, i.e., through an iterative three-step process: (1) identification of potential γ-ray point sources, the "seeds"; (2) optimization of the model of the γ-ray sky describing both the diffuse emission and the potential sources; and (3) the creation of a residual TS map. This iterative process was performed using the pointlike (Kerr 2010) analysis pipeline. We briefly summarize the steps below.

The starting model was the collection of sources in the 2FGL catalog, to which we added the new seeds obtained with the source-search algorithms mr_filter (Starck & Pierre 1998), PGWave (Damiani et al. 1997; Ciprini et al. 2007) and the minimal spanning tree (Campana et al. 2008). Each of the algorithms was applied to γ rays in the 10–500 GeV range in the 3 yr data set, and all seeds found with at least one of these were considered. The initial model was refined by an iterative process in which new seeds were identified in residual TS maps that covered the full sky, and seeds that were no longer significant in the model were removed. The source-search algorithms were not used for the successive iterations. As for the TS maps in 2FGL, the value of TS at any given position was evaluated as the sum of test statistics for separate energy bands, TS_i, spanning the overall energy range.

In each iteration, the locations of the potential sources were optimized during the third step, the creation of the residual TS map. In this step, the log likelihood was maximized with respect to position of each seed, keeping the rest of the model (diffuse emission and other seeds) unchanged.

The uncertainty in the localization of a seed was determined by evaluating the variation of the likelihood function with

Table 1
Extended Sources Modeled in the 1FHL Analysis

1FHL Name	Extended Source	Spatial Form	Extent	Reference
...	SMC	2D Gaussian	0.9	Abdo et al. (2010c)
J0526.6−6825e	LMC	2D Gaussian[a]	1.2, 0.2	Abdo et al. (2010m)
...	S 147	Map	...	Katsuta et al. (2012)
J0617.2+2234e	IC 443	2D Gaussian	0.26	Abdo et al. (2010l)
J0822.6−4250e	Puppis A	Disk	0.37	Lande et al. (2012)
J0833.1−4511e	Vela X	Disk	0.88	Abdo et al. (2010i)
J0852.7−4631e	Vela Junior	Disk	1.12	Tanaka et al. (2011)
...	Centaurus A (lobes)	Map	...	Abdo et al. (2010d)
J1514.0−5915e	MSH 15−52	Disk	0.25	Abdo et al. (2010b)
J1615.3−5146e	HESS J1614−518	Disk	0.42	Lande et al. (2012)
J1616.2−5054e	HESS J1616−508	Disk	0.32	Lande et al. (2012)
J1633.0−4746e	HESS J1632−478	Disk	0.35	Lande et al. (2012)
J1713.5−3951e	RX J1713.7−3946	Map	...	Abdo et al. (2011c)
J1801.3−2326e	W28	Disk	0.39	Abdo et al. (2010h)
J1805.6−2136e	W30	Disk	0.37	Ajello et al. (2012a)
J1824.5−1351e	HESS J1825−137	2D Gaussian	0.56	Grondin et al. (2011)
J1836.5−0655e	HESS J1837−069	Disk	0.33	Lande et al. (2012)
J1855.9+0121e	W44	Ring[b]	(0.22, 0.14), (0.30, 0.19)	Abdo et al. (2010k)
J1923.2+1408e	W51C	Disk[b]	(0.40, 0.25)	Abdo et al. (2009e)
J2021.0+4031e	γ-Cygni	Disk	0.63	Lande et al. (2012)
J2028.6+4110e	Cygnus Cocoon	2D Gaussian	2.0	Ackermann et al. (2011a)
...	Cygnus Loop	Ring	0.7, 1.6	Katagiri et al. (2011)

Notes. List of all sources that have been modeled as extended sources. The Extent column indicates the radius for Disk sources, the disperston for Gaussian sources, and the inner and outer radii for Ring sources. All spectra were modeled as power laws (as for point sources). Four were not detected above 10 GeV and do not have an 1FHL entry.
[a] Combination of two 2D Gaussian spatial templates.
[b] The shape is elliptical; each pair of parameters (a, b) represents the semi-major (a) and semi-minor (b) axes.

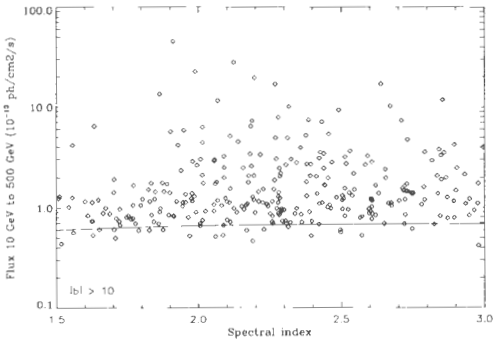

Figure 4. Photon fluxes of all detected sources outside the Galactic plane (|b| > 10°) vs. their photon spectral indices. The theoretical detection threshold for the average background is overlaid as the full line. As a result of the low intensity of the diffuse background and nearly constant PSF width over the entire range the detectability depends only very weakly on the spectral index.

respect to the best-fit position. To define the 95% source location uncertainty region we fit an ellipse to the likelihood surface about the maximum, with offset $2\Delta \log L = -5.99$. The eccentricities of the source-location regions are moderate, averaging 0.47, corresponding to a semi-minor-to-semi-major axis ratio of 0.89. The ellipses have no preferred orientation on the sky. The average solid angle of the 95% confidence regions correspond to an effective position uncertainty of 0.09: the range is 0.01–0.22.

For 1FHL we have not applied corrections for systematic uncertainties for the source location region sizes. As we show in Section 3.4, for the 416 sources with firmly established associations and no spatial extension in LAT or IACT measurements, 19 (4.5%) of the associations lie outside their calculated 95% source location regions. This is consistent with the nominal expectation, especially in consideration of the potential for slight bias from the role of angular offsets in assigning associations. For the 2FGL catalog analysis the systematics on source locations were somewhat larger, and a scale factor of 1.1 was applied. For 2FGL the formal source location regions of the brightest pulsars were quite small and 0.005 was added in quadrature to account for potential residual misalignment of the LAT and spacecraft. For the 1FHL catalog, this factor would have, at most, a minor contribution to all source location region sizes so we have not included it.

3.2. Spectral Analysis of the Candidate Sources

Starting from the list of seeds (Section 3.1), we divided the sky into a number of regions of interest (RoIs) covering all source seeds; 561 RoIs were used for 1FHL. Each RoI extends 2° beyond the seeds that are to be optimized within it in order to cover the entire PSF as well as allow the background diffuse emission to be well fit. Because the spatial resolution is good above 10 GeV, there is little cross-talk between sources or between RoIs, so global convergence was relatively easy to achieve.

We explicitly model the known spatially extended sources as extended, using the spatial extension from energies below 10 GeV, as reported in previous works. In addition to the 12 extended sources included in the 2FGL analysis, we also included 10 that have been detected as extended sources since then. Table 1 lists the source names, spatial template descriptions, and references for the dedicated analyses of these sources. The 18 of these sources that are detected significantly (TS > 25) above

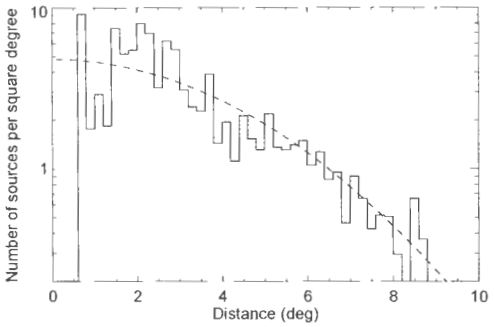

Figure 5. Distribution of nearest neighbor angular distances D_n for all detected sources with $|b| > 10°$. Each entry is scaled by $2\pi D_n \Delta D_n$, with $\Delta D_n = 0.2$ the width of the bin in angular separation, in order to scale out solid-angle effects. The dashed curve indicates the expected Gaussian distribution that would result for a random distribution of sources with no confusion.

10 GeV are tabulated with the point sources, with the only distinction being that no position uncertainties are reported (see Section 4).

Over the relatively narrow range 10–500 GeV, no source was found to have significant spectral curvature, so each spectrum was described by a power-law model. Each RoI is too small to allow both the Galactic and isotropic diffuse components to be properly characterized, so the isotropic level was fixed to the best-fit value over the entire sky and we left free the Galactic normalization only.

This analysis was performed with the ScienceTools software package version v9r26p02. We used binned likelihood functions, as in 2FGL, handling Front and Back events separately, with 0.05 and 0.1 spatial binning respectively, and 10 energy bins per decade. The detection threshold was set to TS > 25, corresponding to a significance just over 4σ for 4 degrees of freedom (two for the localization, and two for the spectrum). Sources below that threshold were discarded from the model, except for the extended sources, which we retained to model the background even when they were not clearly detected above 10 GeV. No constraint was enforced on the minimum number of γ rays from detected sources, because above 10 GeV and outside the Galactic plane the detection is not background limited. In practice the faintest sources were detected with only 4 γ rays.

At the end of the process 514 sources (including 18 of the extended sources that we introduced manually) remained at TS > 25 among the 1705 input seeds. The photon and energy fluxes over the full energy range were obtained by integrating the power-law fits and propagating the errors. The fluxes and spectral indices of the high-latitude sources ($|b| > 10°$) are shown in Figure 4.

Owing to the good angular resolution above 10 GeV (see Section 2.2), and the relatively low density of sources (in comparison with 2FGL), the detection of these sources is less affected by source confusion than was the case in the 2FGL catalog analysis. Figure 5 shows that the distribution of nearest-neighbor source separations for $|b| > 10°$ is consistent with isotropic down to separations of ~0.5. For the 2FGL analysis, source confusion became noticeable at ~1°. From fitting the observed distribution of nearest neighbor separations for separations greater than 1°, for which source confusion is not a consideration, we estimate that 5 sources were missed owing to source confusion, corresponding to a fraction of missed sources of 1.2%.

After that global fitting over the full energy range we extracted photon fluxes in three energy bands: 10–30 GeV, 30–100 GeV and 100–500 GeV. These were obtained in the same way as fluxes in the 2FGL catalog, by holding fixed all spectral indices and adjusting the normalizations only, including the Galactic diffuse. We checked that the sum of photon fluxes is very well correlated with the overall flux from the power-law fit. There is more scatter on the energy flux, which depends more on the highest energy band where the statistical uncertainties are largest.

Many sources, particularly above 100 GeV, are deep in the Poisson regime (just a few events). As a result the likelihood profile is very asymmetric, falling steeply from the maximum toward low fluxes but more gently toward large fluxes. In order to reflect that situation in the catalog data products we report separate 1σ error bars toward low and high fluxes for individual bands, obtained via MINOS in the Minuit[85] package. When the test statistic in the band $TS_i < 1$ the 1σ interval contains 0, and in that case the negative error is set to Null. For these non-significant sources we extract 95% upper limits obtained using a Bayesian method (following Helene 1983), by integrating $L(F_i)$ from 0 up to the flux that encompasses 95% of the posterior probability. With the probability chosen in this way the 95% upper limits F_{95} are similar to $F_i + 2\Delta F_i$ for a hypothetical source with $TS_i = 1$, where F_i and ΔF_i are the best fit and the 1σ upper error bar obtained from MINOS. Therefore in those cases we report $(F_{95} - F_i)/2$ in the upper error bar, so that this column has approximately the same meaning for all sources.

Figure 6 compares the spectral measurements reported in the 2FGL paper (in the 100 MeV to 100 GeV energy range) with the results reported here in the 10–500 GeV energy range, for four representative sources. 95% upper limits are plotted when $TS_i < 1$, as explained above. In order to convert the photon fluxes in each band to νF_ν we proceeded as follows:

1. We converted the photon fluxes into energy fluxes in the same band, on the basis of the same power-law approximation used in the fit (photon index = Spectral_Index of Table 2).
2. We converted the energy fluxes into νF_ν by dividing by the logarithmic width of the band $\ln(E_{i+1}/E_i)$ where E_i and E_{i+1} are the start and end points of the energy interval.

We applied the same method to the 2FGL points, using the local spectral index at the bin center (in log) for the curved spectra.

The blazar Mrk 180 ($z = 0.046$) has a 1FHL spectrum that is a continuation of its 2FGL spectrum, while the classical TeV blazar PKS 2155−304 ($z = 0.116$), which is a few times brighter than Mrk 180, shows a clear turnover (from hard to soft spectrum) at about 10 GeV. Given that PKS 2155−304 is a relatively nearby source, this turnover is due to an internal break in the emission mechanism of this source. On the other hand, the spectrum of the distant blazar PKS 0420−01 ($z = 0.916$) shows a clear cutoff (strong turnover) around 10 GeV which, given the very high redshift of this source, is likely dominated by the absorption of γ-rays in the extragalactic background light (EBL). The fourth panel of Figure 6 shows the 1FHL spectrum of the high-mass binary system LS 5039, which has a completely different shape with respect to the

[85] http://lcgapp.cern.ch/project/cls/work-packages/mathlibs/minuit/home.html

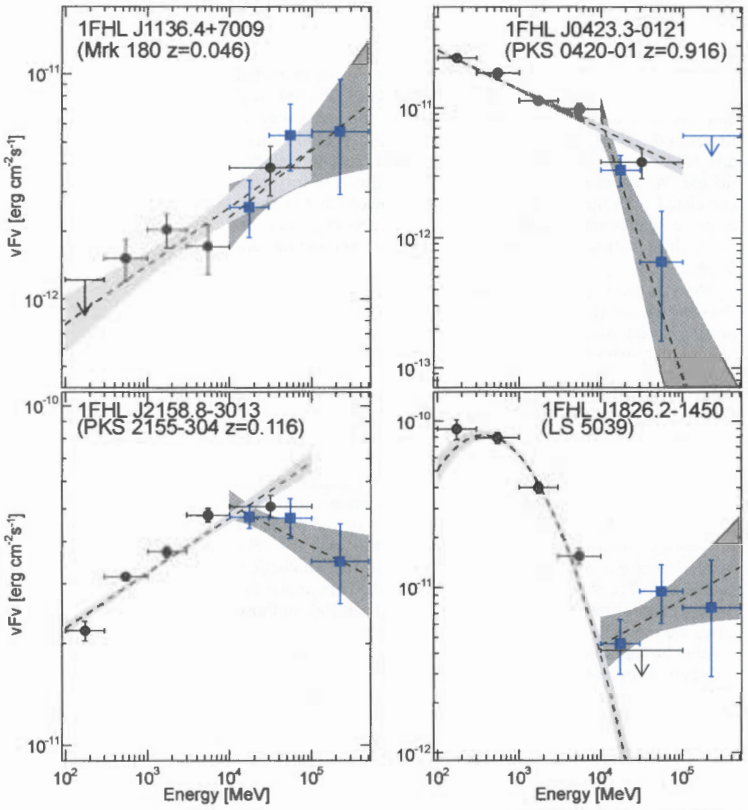

Figure 6. Spectral energy distribution of four representative 1FHL sources with different spectral shapes above 10 GeV: the blazars Mrk 180 (z = 0.046), PKS 2155−304 (z = 0.116), and PKS 0420−01 (z = 0.916), and the high-mass binary system LS 5039. The black circles and light-gray bands depict the results reported in the 2FGL catalog, while the blue squares and the dark-gray bands depict the spectral results reported in this work. The panels are labeled with the 1FHL names and the names of the corresponding associated sources (in parentheses). See text for further details.

(A color version of this figure is available in the online journal.)

2FGL spectrum, hence indicating the presence of a new spectral component (see Hadasch et al. 2012). Such deviations from the simple spectral extrapolation from lower energies indicate the increasing dominance of other physical processes occurring at the source, or in the environment crossed by the γ rays, and hence they are very relevant for the proper understanding of these sources. This is one of the important motivations for producing the 1FHL catalog.

3.3. Quantification of Variability with the Bayesian Block Algorithm

The Bayesian Block algorithm for detecting and characterizing variability in time series data (Scargle 1998; Scargle et al. 2013) is particularly well-suited for analyzing low count data, an important consideration for the 1FHL catalog, for which more than half of the sources have fewer than 20 associated counts. The algorithm partitions the time series data into piecewise constant segments (blocks), each characterized by a rate (or flux) and duration. The locations of the transitions between blocks are determined by optimizing a fitness function for the partitions. The algorithm for finding the optimal partitioning is described by Jackson et al. (2005). For the analysis of the 1FHL data, the fitness function used is the logarithm of the maximum likelihood for each individual block under the constant local rate hypothesis, as described by Scargle et al. (2013). Using the simulation results presented in that paper, an acceptable fraction of false positives for detecting variability can be easily specified. In the analysis presented here, a false positive threshold of 1% was used for all sources. This method also takes into account the effective exposure associated to each event, thus correcting for the exposure variations due to the motion of the field of view of the LAT.

For each source, we used an RoI of 0.°5 radius centered on the best-fit coordinates to extract the events. For sources with neighboring 1FHL sources closer than 1°, we set the radius of the RoI to the greater value of (angular separation/2) or 0.°25. Only five pairs of sources had their RoIs fixed at 0.°25, all of which are located in the Galactic plane. In addition to the Bayesian Block analysis, for each source we also performed an aperture

Table 2
LAT 1FHL FITS Format: LAT_Point_Source_Catalog Extension

Column	Format	Unit	Description
Source_Name	18A	...	...
RAJ2000	E	deg	Right ascension
DEJ2000	E	deg	Declination
GLON	E	deg	Galactic longitude
GLAT	E	deg	Galactic latitude
Conf_95_SemiMajor	E	deg	Long radius of error ellipse at 95% confidence level
Conf_95_SemiMinor	E	deg	Short radius of error ellipse at 95% confidence level
Conf_95_PosAng	E	deg	Position angle of the 95% long axis from celestial north, positive toward increasing RA (eastward)
Signif_Avg	E	...	Source significance in σ units (derived from TS)
Pivot_Energy	E	GeV	Energy at which error on differential flux is minimal
Flux_Density	E	cm^{-2} GeV^{-1} s^{-1}	Differential flux at Pivot_Energy
Unc_Flux_Density	E	cm^{-2} GeV^{-1} s^{-1}	1σ error on differential flux at Pivot_Energy
Spectral_Index	E	...	Best fit photon number power-law index
Unc_Spectral_Index	E	...	1σ error on Spectral_Index
Flux	E	cm^{-2} s^{-1}	Integral photon flux from 10 to 500 GeV
Unc_Flux	E	cm^{-2} s^{-1}	1σ error on integral photon flux from 10 to 500 GeV
Energy_Flux	E	erg cm^{-2} s^{-1}	Energy flux from 10 to 500 GeV obtained by spectral fitting
Unc_Energy_Flux	E	erg cm^{-2} s^{-1}	1σ error on energy flux from 10 to 500 GeV
Flux10_30_GeV	E	cm^{-2} s^{-1}	Integral flux from 10 to 30 GeV
Unc_Flux10_30_GeV	2E	cm^{-2} s^{-1}	1σ errors on integral flux from 10 to 30 GeV[a]
Sqrt_TS10_30_GeV	E	...	Square root of the Test Statistic between 10 and 30 GeV
Flux30_100_GeV	E	cm^{-2} s^{-1}	Integral flux from 30 to 100 GeV
Unc_Flux30_100_GeV	2E	cm^{-2} s^{-1}	1σ errors on integral flux from 30 to 100 GeV[a]
Sqrt_TS30_100_GeV	E	...	Square root of the Test Statistic between 10 and 30 GeV
Flux100_500_GeV	E	cm^{-2} s^{-1}	Integral flux from 100 to 500 GeV
Unc_Flux100_500_GeV	2E	cm^{-2} s^{-1}	1σ errors on integral flux from 100 to 500 GeV[a]
Sqrt_TS100_500_GeV	E	...	Square root of the Test Statistic between 100 and 500 GeV
Variability_BayesBlocks	I	...	Number of Bayesian Blocks[b] found (1 for non-variable)
Extended_Source_Name	18A	...	Cross-reference to the Extended Sources extension for extended sources, if any
ASSOC_GAM	18A	...	Name of corresponding source in gamma-ray catalog, if any
TEVCAT_FLAG	2A	...	P if positional association with non-extended source in TeVCat
		...	E if associated with an extended source in TeVCat, N if no TeV association
		...	C if the source survives the TeV candidate selection criteria specified in Section 5.
ASSOC_TEV	21A	...	Name of TeV association, if any
CLASS1	4A	...	Class designation for most likely association; see Table 4
CLASS2	4A	...	Class designation for alternate association, if any
ASSOC1	26A	...	Name of identified or most likely associated source
ASSOC2	26A	...	Name of alternate association, if any

Notes.
[a] Separate 1σ errors are computed from the likelihood profile toward lower and larger fluxes. The lower error is set equal to Null if the 1σ interval contains 0.
[b] The probability threshold for the Bayesian Blocks analysis is given by the VARPROBA keyword.
(Supplemental data for this table are available in the online journal.)

photometry analysis using 50 equal time bins spanning the 3 yr interval. We did not do any background subtraction in either analysis. Results of the Bayesian Block analysis are presented in Section 4.2.

3.4. Associations

The 1FHL sources were associated with (known) sources at other wavelengths using similar procedures as for the 2FGL and 2LAC (Ackermann et al. 2011b) catalogs. As for these catalogs, we keep the distinction between an association and an identification, the latter being more conservative. Promoting an association to an identification requires that correlated variability or source extension be found with observations at other wavelengths.

The associations were derived with two different procedures: the Bayesian and the likelihood-ratio association methods (de Ruiter et al. 1977; Sutherland & Saunders 1992). The Bayesian method and its implementation for associating LAT sources with potential counterparts at other wavelengths is described in an appendix of the 1FGL paper (Abdo et al. 2010e), and some refinements are reported in the 2FGL paper. The likelihood-ratio method and its implementation are described in the 2LAC paper. In the application of these two methods, potential counterparts were retained as associations if they were found to have a posteriori probabilities of at least 80%.

For the Bayesian method, we used the 13th edition of the Veron catalog (Véron-Cetty & Véron 2010), version 20 of BZCAT (Massaro et al. 2009), the 2010 December 5 version of the VLBA Calibrator Source List,[86] and version 3.400 of the TeVCat catalog. We also added new counterpart catalogs: the Australia Telescope 20-GHz Survey (AT20G) (Murphy et al.

[86] http://astrogeo.org/vcs/

2010; Massardi et al. 2011) and the Planck Early Release Compact Source Catalog (Planck Collaboration et al. 2011).

For the likelihood-ratio method, the catalogs of potential counterparts were the NRAO VLA Sky Survey (Condon et al. 1998), the second version of the wide-field radio imaging survey of the southern sky (Mauch et al. 2003), the PMN-CA catalog of southern radio sources (Wright et al. 1996), and the ROSAT all-sky survey bright source catalog (Voges et al. 1999). Note that these catalogs contain mostly extragalactic sources and so the likelihood-ratio method was not very efficient in associating 1FHL sources with Galactic sources.

In addition, we also evaluated correspondences with the 2FGL and 1FGL catalogs of LAT sources, and gave them higher priorities with respect to the other (non-Fermi) catalogs. Therefore, whenever possible, we associated the 1FHL sources to previously cataloged LAT sources, and for these cases we also adopted the source associations given in the previously published Fermi catalogs.

The sources that could be associated with known or previously reported sources (including unassociated 2FGL and 1FGL objects) total 484, of which 451 could be associated with 2FGL sources, and 11 with 1FGL sources that are not in the 2FGL catalog. We note that the number of 1FHL sources associated by the Bayesian method is 484, while the number that were associated using the likelihood-ratio method is 441 (all of which were also associated with the Bayesian method). This difference in performance is attributable to the likelihood-ratio method being used only to find associations with extragalactic sources, while the Bayesian method is more general and used specific catalogs of Galactic sources. Three 1FHL sources each have associations with two distinct sources with posterior probabilities greater than 80%: 1FHL J0217.4+0836 (associated with a BL Lac object and an FSRQ), 1FHL J0323.5−0107 (associated with two distinct BL Lac objects), and 1FHL J0442.9−0017 (associated with a FSRQ and a BL Lac object). We also note that the 1FHL catalog contains 52 (= 514 − 451 − 11) sources that could not be associated to objects reported in previous LAT catalogs (with 11 months and 2 yr of accumulated data for 1FGL and 2FGL respectively). We describe these in Section 4.

4. THE 1FHL CATALOG

This section describes the contents of the 1FHL catalog and reports the basic properties of the 1FHL sources. The collective properties of the sources that do not have counterparts in the 2FGL catalog, the sources that are associated with AGNs, and the pulsars emitting above 10 GeV are also discussed.

4.1. Description of the 1FHL Catalog

Table 2 describes the full contents of the 1FHL catalog data product, which is available in FITS format from the FSSC. Table 3 presents the catalog itself. Column names are identical (when the meaning is the same) or similar to 2FGL columns (Nolan et al. 2012). The main exception is the Variability_BayesBlocks entry which is computed from the Bayesian Blocks analysis (Section 3.3). The γ-ray association column lists the corresponding source, if any, in the 2FGL, 1FGL, 3EG, or EGR (Casandjian & Grenier 2008) catalogs. Of the 46 high-confidence sources in the Lamb & Macomb (1997) GEV catalog of EGRET sources detected above 1 GeV, 35 have associations with 1FHL sources. For the 1FHL catalog the source designations are 1FHL JHHMM.m± DDMM, where FHL stands for Fermi High-energy (source) LAT, where high energy means above 10 GeV.

The designators for the source associations and identifications are listed in Table 4 along with the source counts. Because of the limited capability for variability and morphological studies (due to the low photon counts above 10 GeV), for 1FHL sources with counterparts in the 2FGL catalog we adopted the same associations and identifications as for 2FGL. Similarly we also used the designator "spp" to denote the class of the six sources that have positional associations with supernova remnants (SNRs) of angular diameters $> 20^{\square}$ and/or pulsar wind nebulae (PWNe). Owing to the increased chance of coincidental associations with the SNRs and the ambiguity of SNR versus PWN associations for some of the sources, the potential associations are reported separately, in Table 5. Only two new class designators were included in the 1FHL catalog. For 20 pulsars, pulsed emission was detectable above 10 GeV (see Section 4.5), and we use "HPSR" as the class designator. Also, we use the designator "SFR," for star-forming region, and apply it to the Cygnus Cocoon (1FHL J2028.6+4110e).

A remarkable characteristic of this catalog is that the blazars and blazar candidates[87] amount to ~75% of the entire catalog (~86% of the associated sources), indicating that this source class largely dominates the highest-energy LAT sky. It is worth mentioning that the four 1FHL sources associated with radio galaxies have also shown characteristics that are typical for blazars, either in radio morphology (prominent flat-spectrum core with one-sided jet), in optical spectrum, or in γ-ray variability (sporadic short-term flux variability with timescales of $\square$1 day). This is the case for PKS 0625−35 (e.g., see Wills et al. 2004), M 87 (e.g., see Abramowski et al. 2012), NGC 1275 (e.g., see Kataoka et al. 2010; Aleksić et al. 2012a), and IC 310 (e.g., see Kadler et al. 2012; Shaw et al. 2013; The MAGIC Collaboration et al. 2013). The fifth radio galaxy, Cen A, is exceptional because of its proximity and also a presence of γ-ray emitting giant lobes clearly resolved with the LAT (Abdo et al. 2010d). Blazar-like properties of the active nucleus in the source, which has been also detected in the VHE band (Aharonian et al. 2009), are subject to ongoing debate. The only non-AGN extragalactic source is the nearby Large Magellanic Cloud (LMC) galaxy, which, given its proximity, has an extension of 2°.

The second largest source class is pulsars, with 5.2% of the catalog total. SNRs and PWNe together are only 4.5% of the catalog.

We note that, of the 65 1FHL sources that could not be associated with sources of known natures, five are associated with extended (Galactic) unidentified H.E.S.S. sources, 26 are associated with unidentified 2FGL sources (including 1 associated with one of the five previously mentioned Galactic H.E.S.S. unidentified sources), 5 are associated with unidentified 1FGL sources, and 2 are associated with unidentified sources from the 3EG catalog. The remaining 28 sources could not be associated with any γ-ray source reported previously. We note that the fraction of unassociated 1FHL sources is only ~13% (65 out of 514), while that of the unassociated 2FGL sources was ~31% (575 out of 1873). The smaller fraction of unassociated 1FHL sources might be related to the lower source density and good source localization, which facilitates the association of the sources, as well as the brightness of the 1FHL sources at lower

[87] The fraction of non-beamed AGNs is expected to be only a few percent, and so most of the AGNs of unknown type are expected to be blazars of either FSRQ or BL Lac type.

Table 3
LAT Catalog of Sources above 10 GeV

Name 1FHL	R.A.	Decl.	l	b	θ_1	θ_2	φ	σ	F_{10}	ΔF_{10}	S_{10}	ΔS_{10}	Γ_{10}	$\Delta\Gamma_{10}$	Var	γ-ray Assoc.	TeV	Class	ID or Assoc.
J0007.3+7303	1.827	73.060	119.682	10.467	0.024	0.023	−9	31.8	125.1	10.3	31.6	3.1	3.73	0.24	1	2FGL J0007.0+7303	E	HPSR	LAT PSR J0007+7303
J0007.7+4709	1.947	47.155	115.271	−15.067	0.073	0.058	43	7.1	14.5	4.1	3.8	1.3	3.57	0.74	1	2FGL J0007.8+4713	···	bzb	MG4 J000800+4712
J0008.7−2340	2.194	−23.674	50.306	−79.770	0.120	0.114	−65	4.5	8.2	3.4	3.2	2.0	2.57	0.69	1	2FGL J0008.7−2344	···	bzb	RBS 0016
J0009.2+5032	2.316	50.541	116.110	−11.772	0.075	0.066	−88	10.6	27.2	5.4	12.3	3.8	2.38	0.30	1	2FGL J0009.1+5030	C	bzb	NVSS J000922+503028
J0018.6+2946	4.673	29.776	114.500	−32.559	0.144	0.121	−60	4.6	7.5	3.1	4.7	3.1	2.02	0.49	1	2FGL J0018.5+2945	C	bzb	RBS 0042
J0022.2−1853	5.555	−18.899	82.190	−79.380	0.083	0.068	39	7.0	12.2	4.1	9.2	4.9	1.85	0.37	1	2FGL J0022.2−1853	C	bzb	1RXS J002209.2−185333
J0022.5+0607	5.643	6.124	110.019	−56.023	0.119	0.108	−22	6.3	14.1	4.5	5.7	2.7	2.53	0.51	1	2FGL J0022.5+0607	C	bzb	PKS 0019+058
J0030.1−1647	7.525	−16.797	96.297	−78.550	0.118	0.092	74	4.3	5.6	2.8	5.9	4.7	1.56	0.50	1	···	C	···	···
J0033.6−1921	8.407	−19.361	94.245	−81.223	0.047	0.044	−55	15.4	42.0	7.3	28.9	8.2	1.93	0.21	1	2FGL J0033.5−1921	P	bzb	KUV 00311−1938
J0035.2+1514	8.806	15.234	117.143	−47.455	0.079	0.071	−77	6.9	14.6	4.4	5.2	2.2	2.73	0.54	1	2FGL J0035.2+1515	···	bzb	RX J0035.2+1515
J0035.9+5950	8.990	59.838	120.987	−2.975	0.043	0.039	−19	13.3	34.9	6.0	29.8	8.0	1.74	0.19	1	2FGL J0035.8+5951	P	bzb	1ES 0033+595
J0037.8+1238	9.473	12.645	117.778	−50.091	0.113	0.098	−18	4.3	7.1	3.1	2.1	1.2	3.22	0.96	1	2FGL J0037.8+1238	···	bzb	NVSS J003750+123818

Notes. R.A. and Decl. are celestial coordinates in J2000 epoch, l and b are Galactic coordinates, in degrees; θ_1 and θ_2 are the semi-major and semi-minor axes of the 95% confidence source location region; φ is the position angle in degrees east of north; F_{10} and ΔF_{10} are photon flux (10–500 GeV) in units of 10^{-11} cm^{-2} s^{-1}; S_{10} and ΔS_{10} are the energy flux (10–500 GeV) in units of 10^{-12} erg cm^{-2} s^{-1}; Γ_{10} and $\Delta\Gamma_{10}$ are the photon power-law index and uncertainty for a power-law fit; Var is the number of change points in the Bayesian Blocks light curve (see the text); γ-ray Assoc. lists associations with other catalogs of GeV γ-ray sources; TeV indicates an association with a point-like or small angular size TeV source (P) or extended TeV source (E); this column also indicates good candidates for TeV detections (C), as defined in Section 5; Class designates the astrophysical class of the associated source (see the text); ID or Assoc. lists the primary name of the associated source or identified counterpart. Three 1FHL sources have two associations listed here, the two distinct associated source names and class types are reported separated by the symbol "&."

(This table is available in its entirety in a machine-readable form in the online journal. A portion is shown here for guidance regarding its form and content.)

Table 4
LAT 1FHL Sources by Class

Class Description	Identified Designator	Number	Associated Designator	Number	Total Number	Fraction of Full Catalog (%)
Blazar of the BL Lac type	BZB	7	bzb	252	259	50.4
Blazar of the FSRQ type	BZQ	13	bzq[a]	58	71	13.8
Active galaxy of uncertain type	AGU	1	agu	57	58	11.3
Pulsar, identified by pulsations above 10 GeV	HPSR	20	...	...	20	3.9
Pulsar, identified by pulsations in LAT (excluding HPSR)	PSR	6	...	...	6	1.2
Pulsar, no pulsations seen in LAT yet	...	...	psr	1	1	0.2
Supernova remnant	SNR	6	snr	5	11	2.1
Pulsar wind nebula	PWN	3	pwn	3	6	1.2
Unclear whether SNR or PWN	...	...	spp	6	6	1.2
Radio galaxy	RDG	1	rdg	4	5	1.0
High-mass binary	HMB	3	hmb	0	3	0.6
Normal galaxy	GAL	1	gal	0	1	0.2
Star forming region	SFR	1	sfr	0	1	0.2
LBV star	LVB	0	lvb	1	1	0.2
Unassociated source	...	...	...	65	65	12.6

Notes. For the three 1FHL sources with two associations (see Section 3.4 and Table 3), we consider only the first associated source (which is the one with the highest probability of association).
[a] 1FHL J1312.8+4827, classified here as bzq, may in fact be a narrow-line Seyfert 1 galaxy (Sokolovsky et al. 2013).

Table 5
Potential Associations for Sources Near SNRs

1FHL Name	2FGL Name	SNR Name	PWN Name	TeV Name	Common Name
J1111.5−6038	J1112.1−6040	G291.0−00.1	G291.0−0.1	...	...
J1552.6−5610	J1552.8−5609	G326.3−01.8	...	...	Kes 25
J1640.5−4634	J1640.5−4633	G338.3−00.0	G338.3−0.0	HESS J1640−465	...
J1717.9−3725	J1718.1−3725	G350.1−00.3	...	...	...
J1745.6−2900	J1745.6−2858	G000.0+00.0	G359.98−0.05	...	Sgr A East
J1834.6−0703	J1834.7−0705c	G024.7+00.6	...	...	...

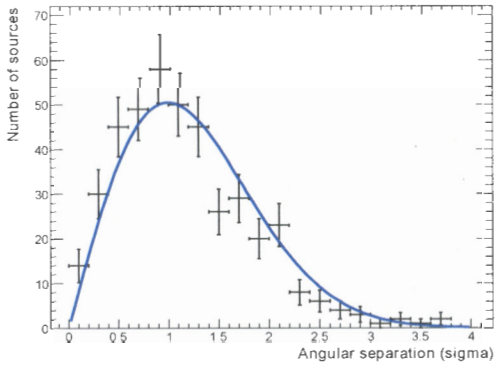

Figure 7. Distribution of the angular separation between the 1FHL sources and the objects with which they are associated. Only point sources were included in this distribution. The angular separation is normalized with the quantity $r_{95}/\sqrt{-2\ln 0.05}$, where r_{95} is the location uncertainty at the 95% confidence level. The blue curve is the expected distribution of real associations. See text for details.

(A color version of this figure is available in the online journal.)

frequencies (particularly optical and X-ray) in comparison to that of the 2FGL sources.

Figure 7 shows the distribution of angular separations between the associated 1FHL sources and their counterparts. The total number of sources shown in this distribution is 416. Of the 449 1FHL sources with associations, we removed the 16 1FHL extended sources (see Table 1),[88] the 6 sources classified as "spp" (see Table 5), and 11 1FHL sources that are positionally coincident with extended TeV sources (all of which are γ-ray pulsars: 5 PSR and 6 HPSR). These 33 sources were removed because the emission centroid in one energy range does not necessarily coincide with the centroid (or location for point sources) in the other energy range. The angular separation for each source was normalized with the quantity $r_{95}/\sqrt{-2\ln 0.05}$, where $r_{95} = \sqrt{\theta_1\theta_2}$ is the geometric mean of θ_1 and θ_2, the semi-major and semi-minor radii of the location ellipse at 95% confidence level. The expected distribution of the angular difference with respect to the real associations, when the distances are normalized as described above, is described by a Rayleigh function with $\sigma = 1$. This function is also depicted in Figure 7. The agreement between this model curve and the observed distribution is quantified by a $\chi^2/\mathrm{NDF} = 27/19$ (p-value = 0.10), implying a successful association of the 1FHL sources.

The locations on the sky of the sources in the above-mentioned classes are depicted in Figure 8. To a good approximation, the Galactic sources are located essentially in the Galactic plane (apart from some pulsars), while the blazars are distributed roughly uniformly outside the Galactic plane. The source statistics are relatively low, which precludes strong statements on the source distributions. However, when considering the blazars, which constitute the majority of 1FHL sources, an

[88] Two of the 18 1FHL extended sources are unassociated, and so are not included in the initial sample of 449 sources.

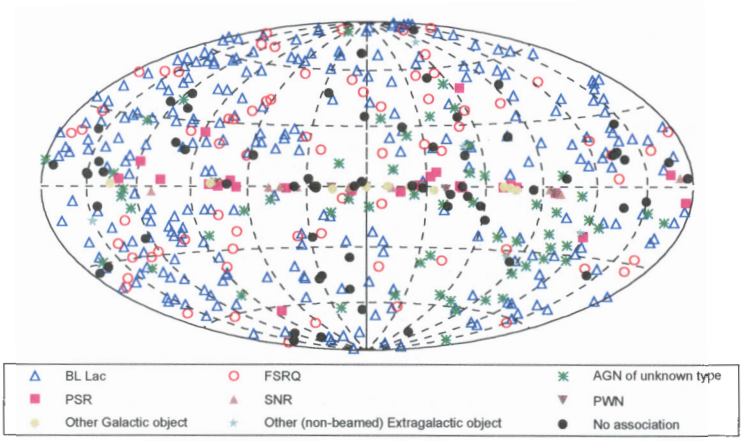

Figure 8. Sky map showing the sources by their source class, as reported in Table 4. The projection is Hammer–Aitoff in Galactic coordinates.
(An extended color version of this figure is available in the online journal.)

asymmetry between the northern and southern Galactic hemispheres seems evident: the number of BL Lac objects and FSRQs is larger in the northern hemisphere, while the number of AGNs of unknown types seems to be larger in the southern hemisphere. The Galactic latitude distributions for these source classes are depicted in Figure 9, showing that the fraction of BL Lac objects and FSRQs in the southern hemisphere is 42% (108 sources out of 259) and 39% (28 sources out of 71) respectively. The fraction of AGNs of unknown type in the southern hemisphere is 71% (41 out of 58), suggesting that many of these sources must be BL Lac objects and/or FSRQs.

A similar north/south asymmetry with a larger number of sources was previously observed and reported in 2LAC and attributed to the slightly different exposure and the known non-uniformities of the counterpart catalogs. In this work, we also consider AGNs with $|b| < 10^{\circ}$ (which were excluded from the 2LAC paper), and they show another asymmetry: the fraction of known BL Lac objects and FSRQs is smaller at low latitudes, while the number of AGNs of unknown type is slightly higher (at the level of 2 standard deviations). The lower fraction of BL Lac objects and FSRQs at low Galactic latitudes is certainly affected by the lower sensitivity of LAT to detect sources in this region due to the higher diffuse background (see Figure 3). Yet in this work we find that the asymmetry in the counterpart catalogs must also play a role in the lower fraction of blazars at low Galactic latitudes, as indicated by the higher fraction of AGNs of unknown type for these latitudes.

The unassociated sources are fairly uniformly distributed outside the Galactic plane, with a substantial increase in density for $|b| < 11^{\circ}.5$ ($|\sin b| < 0.2$). It is to be expected that a large fraction of the low-latitude unassociated sources are pulsars, SNRs and PWNe; but given the distributions shown in Figure 9, unassociated blazars are undoubtedly also present at low Galactic latitudes.

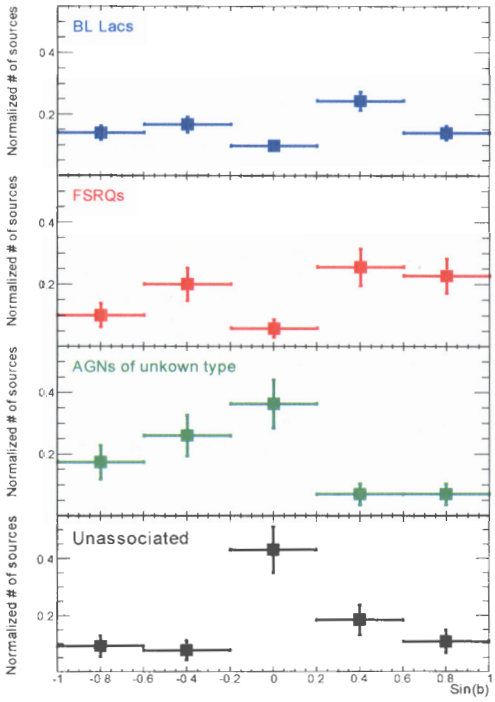

Figure 9. Galactic latitude distributions of BL Lac, FSRQs, AGNs of unknown type, and unassociated 1FHL sources. The distributions were normalized to the total numbers of source associations in each of these source classes, namely 259, 71, 58, and 65, respectively.
(A color version of this figure is available in the online journal.)

4.2. Basic Properties of the 1FHL Sources

Figure 10 shows the distribution of significances (σ, derived from the TS values on the assumption of four degrees of freedom) for the 1FHL sources grouped as extragalactic, Galactic,

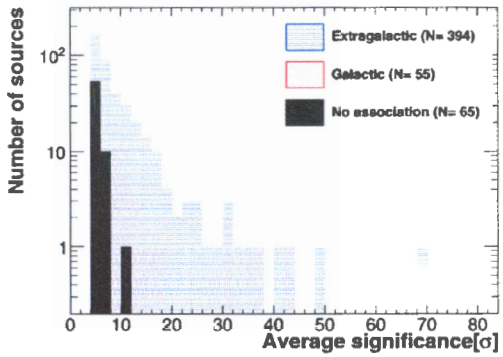

Figure 10. Distribution of the significances of the 1FHL sources. The three histograms report the significances for three groups of sources: extragalactic, Galactic, and unassociated sources.

(A color version of this figure is available in the online journal.)

and unassociated sources. There are no big differences between extragalactic and Galactic. In contrast, the sources without associations differ from those with associations; they are clustered at the lowest significances, with most of them showing a significance smaller than 8σ.

Figure 11 shows the distribution of the measured photon fluxes and photon indices for the various source classes from the 1FHL list, grouped as in Figure 10. Three sources with very soft spectral indices stand out: 1FHL J2311.0+3425 (index 11 ± 5), 1FHL J1907.7+0600 (index 7 ± 2), and 1FHL J1635.0+3808 (index 6 ± 2). The first and third are associated with distant FSRQs (B2 2308+34 and 4C +38.41, both with $z \sim 1.8$), while the second is associated with a γ-ray pulsar (LAT PSR J1907+0602). These three sources are significantly detected in the 10–30 GeV range, but not detected in the ranges 30–100 GeV and 100–500 GeV. Consequently, the spectra resulting from our analysis are extremely soft, and have large statistical uncertainties due to the lack of high-energy photons.

The distribution of spectral indices for 1FHL sources with associations in the Milky Way have no obvious differences from those with blazar associations, while the measured fluxes for the Galactic sources clearly tend to be greater. (The lowest fluxes are found only for sources with extragalactic associations, or no associations.) This is not an intrinsic property of the Galactic sources, but rather due to the worse photon flux sensitivity in the Galactic plane (due to the brighter diffuse backgrounds), as reported in Section 2.4.

A search for variability was performed using the Bayesian Block algorithm as described in Section 3.3. A total of 43 sources show evidence for variability, i.e., have two or more blocks, and they all belong to the blazar class. For these sources, the numbers of events within the RoIs range from 10 (1FHL J0210.9−5100 and 1FHL J1635.0+3808) to 178 (1FHL J0222.6+4302), with a median value of 30. Most of the light curves for the variable sources (39/43) contain two or three blocks, while the light curves for the remaining 4 (4/43) contain four, five, six, and ten blocks each. The number of Bayesian Blocks measured for each of the 1FHL sources is reported in Section 4.4. With our chosen false-positive rate, a total of five to six sources would be expected to have more than 1 block by chance.

Figure 12 shows the light curves of nine sources with different variability characteristics representative of the larger sample. Five of these sources are particularly interesting:

1. The light curve of 1FHL J0222.6+4302 (3C 66A) displays two prominent flares. The first flare occurred in 2008 October and was detected in the VHE band by VERITAS (Swordy 2008; Abdo et al. 2011b). The second flare occurred in 2009 May, but the source was too close to the Sun for VHE observations.
2. The source 1FHL J0238.7+1639 (AO 0235+164) was detected in a high state during the first three months of the Fermi mission before transitioning to a lower state and eventually fading below the threshold for detection after 2009 September.
3. The most frequently variable source in the catalog is 1FHL J1224.8+2122 (4C +21.35). The Bayesian Block algorithm detected ten blocks, indicating four short and strong flares over the course of a few months. No events were detected from this source before 2009 March 1. The second flare was detected above 100 MeV by the Fermi LAT in 2010 April (Donato 2010). The third flare is the brightest detected by the Bayesian Block analysis and occurred on 2010 May 25 when three γ rays (above 10 GeV) were detected within a ten hour span. This flare was reported by AGILE above 100 MeV (Bulgarelli et al. 2010). The last flare occurred between 2010 June 17 and 2010 June 19, when seven γ-ray-like events arrived within a 29 hr interval. It was detected by

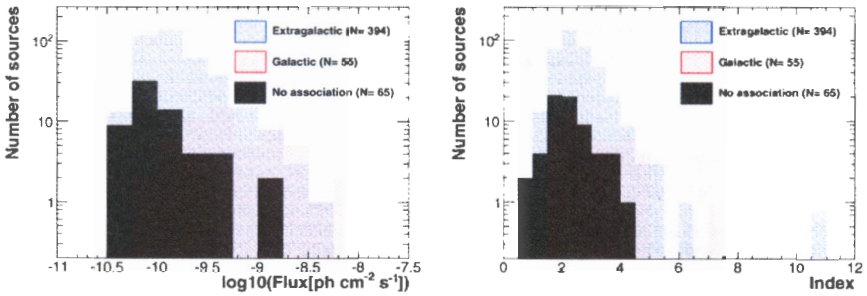

Figure 11. Distribution of the measured photon fluxes (left) and photon index (right) for the 1FHL sources. The three histograms report the significances for three different groups of sources: extragalactic, Galactic and sources without associations.

(A color version of this figure is available in the online journal.)

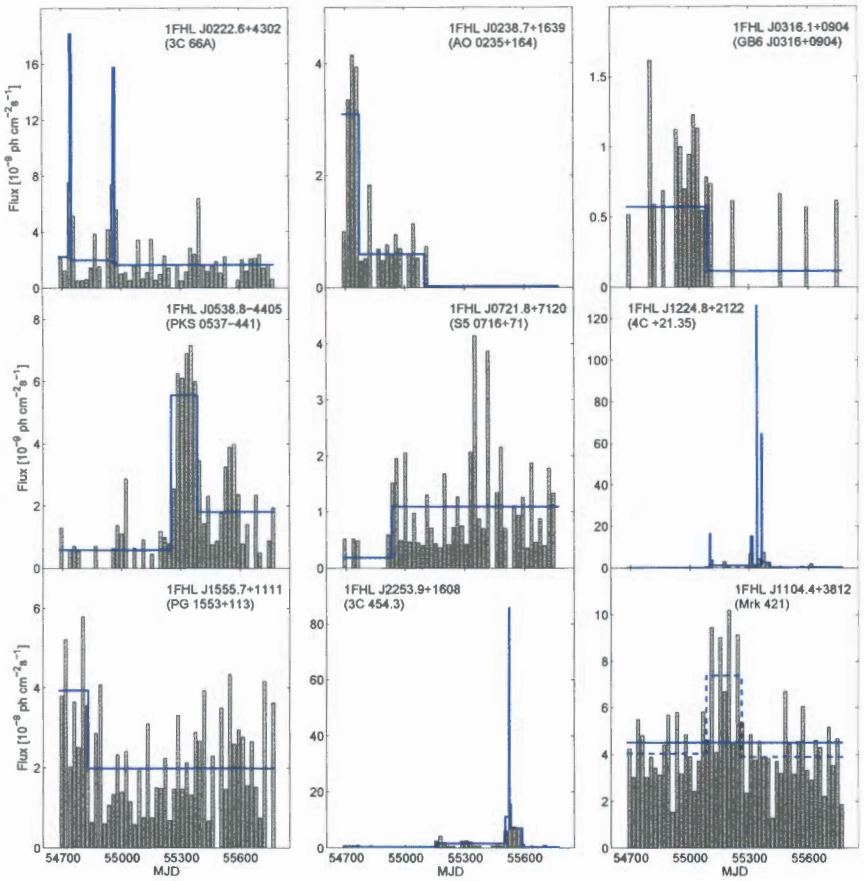

Figure 12. Light curves for a subset of the variable sources. The histograms correspond to the aperture photometry analysis, and the solid lines correspond to the Bayesian Block analysis using a 1% false positive threshold. The panels are labeled with the 1FHL names and the names of the corresponding associated sources (in parentheses). The dashed line in the panel for Mrk 421 corresponds to a 5% false positive threshold (see text for details).

(A color version of this figure is available in the online journal.)

AGILE (Striani et al. 2010b) and Fermi LAT (Iafrate et al. 2010) above 100 MeV. The high activity from this flare was also observed at VHE on 2010 June 17 by MAGIC (Mariotti 2010; Aleksić et al. 2011). MAGIC detected significant variability with a flux-doubling time of only 10 minutes.

4. The source 1FHL J2253.9+1608 (3C 454.3) is among the brightest detected above 10 GeV. A higher-flux state starting in 2010 November and lasting 3 months was detected in both the Bayesian Block and aperture photometry analyses. A short and bright flare occurred during this period starting on 2010 November 19 and lasting only two days. This short/bright flare above 10 GeV is very similar to those observed from 4C +21.35, indicating that the FSRQ 3C 454.3 might also have been detected at VHE had it been observed during this period. However, detection of 3C 454.3 would have been more difficult due to its strong spectral break at GeV energies, even during large flares (see Ackermann et al. 2010; Abdo et al. 2011a) and the greater redshift ($z = 0.859$) of this source. The flare above 10 GeV was also detected above 100 MeV by Fermi LAT (Sanchez & Escande 2010) and AGILE (Striani et al. 2010a).
5. One of the brightest sources in the 1FHL catalog is the high-frequency-peaked blazar 1FHL J1104.4+3812 (Mrk 421). Despite having 383 events within the RoI, the source is not detected as variable by the Bayesian Block analysis above 10 GeV (see Figure 12). The aperture photometry indicates a period of higher activity centered around late 2009 to early 2010. A dedicated analysis with a false positive threshold of 5% confirms this higher flux state, which matches well the period of enhanced VHE activity observed by MAGIC and VERITAS in 2009 November, and 2010 January, February and March (Galante 2011; Sun et al. 2012). However, our variability analysis above 10 GeV fails to detect the extremely bright, day-long VHE flare

Table 6
1FHL Extended Sources Without 2FGL Counterparts

1FHL Name	R.A. (deg)	Decl. (deg)	σ	Extended Source	ASSOC_TEV	CLASS1	2FGL Name	R.A. (2FGL) (deg)	Decl. (2FGL) (deg)	σ (2FGL)	Ang. Sep. (deg)
J2021.0+4031e	305.270	40.520	15.7	gamma Cygni	VER J2019+407	snr	J2021.5+4026	305.392	40.441	129.7	0.12
J0852.7−4631e	133.200	−46.520	11.1	Vela Junior	RX J0852.0−4622	snr	J0851.7−4635	132.941	−46.592	5.5	0.19
J1633.0−4746e	248.250	−47.770	10.9	HESS J1632−478	HESS J1632−478	pwn	J1632.4−4753e	248.114	−47.891	8.8	0.15
J1615.3−5146e	243.830	−51.780	10.8	HESS J1614−518	HESS J1614−518		J1615.2−5138	243.801	−51.635	14.7	0.15
J1713.5−3951e	258.390	−39.850	8.3	RX J1713.7−3946	RX J1713.7−3946	SNR	J1712.4−3941	258.111	−39.687	5.1	0.27
J1616.2−5054e	244.060	−50.910	7.8	HESS J1616−508	HESS J1616−508	pwn	J1615.0−5051	243.758	−50.852	15.2	0.20
J1836.5−0655e	279.140	−6.920	7.6	HESS J1837−069	HESS J1837−069		J1837.3−0700e	279.347	−7.011	8.2	0.22
J0822.6−4250e	125.660	−42.840	6.9	Puppis A		snr	J0823.0−4246	125.766	−42.770	10.2	0.10
J1634.7−4705	248.690	−47.089	4.2		HESS J1634−472		J1635.4−4717c	248.850	−47.297	7.7	0.24

Notes. The entries are sorted in reverse order of detection significance reported in the main 1FHL catalog Table 3. Each of the sources is associated with an extended (Galactic) VHE source. All were classified as point sources in the 2FGL catalog, while 8 (out of 9) were recently found to have a significance extension at MeV/GeV energies, as we noted in Table 1. For these 8 sources, the table reports the Extended_Source_Name used in Table 1.

detected by VERITAS on 2010 February 17, when Mrk 421 increased its flux by about a factor of 20 with respect to its typical value (Ong 2010).

The results from the Bayesian Block analysis cannot be directly compared with the likelihood analysis performed to derive monthly light curves for the 2FGL catalog. Despite the differences in the methods and the time intervals (2 yr versus 3 yr), we highlight some comparisons. Of the 43 variable sources detected above 10 GeV, only 2 sources do not have counterparts in 2FGL (1FHL J0318.8+2134 and 1FHL J1532.6−1317). Both sources show higher fluxes in the third year, i.e., after the time interval of the 2FGL analysis. Of the remaining 41 sources, only 5 did not show evidence for variability in 2FGL (1FHL J0203.6+3042, 1FHL J0316.1+0904, 1FHL J0809.8+5217, 1FHL J1603.7−4903, and 1FHL J1748.5+7006). Therefore, it appears that the population of sources variable above 10 GeV is also variable in the 2FGL energy band (100 MeV–100 GeV). Although the most frequently variable source above 10 GeV (1FHL J1224.8+2122) has the second largest TS_{var} (13030) in 2FGL, the number of Bayesian Blocks and TS_{var} are not strongly correlated. For example, several sources with two or three blocks have much larger TS_{var} values than sources with four, five, or six blocks.

4.3. 1FHL Sources Not in the 2FGL Catalog

The 1FHL catalog Table 3 contains 63 sources not associated with 2FGL sources.[89] Among these sources, spatial extension at MeV/GeV/TeV energies has been recently reported for nine. For eight of these, extension had previously been resolved by the LAT (see Table 1). The nine sources are listed in Table 6. In the 2FGL catalog, each of these sources is modeled as a point source, and as a result our association pipeline failed to link these 1FHL sources with the 2FGL counterparts despite angular separations of less than 0.3 (typically less than 0.2). For this reason, we split the list of 63 non-2FGL sources into two groups: non-2FGL_a, the 9 sources reported in Table 6; and non-2FGL_b, the remaining 54 (point-like) sources without 2FGL counterparts.

Figure 13 shows the distribution of the detection significances for all of the 1FHL sources, grouped in several classes: all sources, sources with 2FGL counterparts, and the two groups of non-2FGL sources described in the text, non-2FGL_a and non-2FGL_b. The distribution peaks at the threshold of ~4σ (TS = 25), and extends to about 40σ with three sources having formal significances greater than 50σ. This plot shows that the γ-ray sources that were not reported in the 2FGL catalog cluster at the significance threshold.

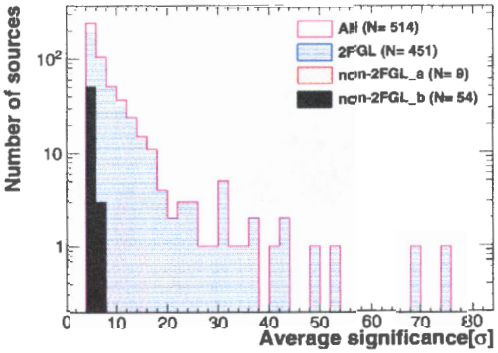

Figure 13. Distribution of the significances of the 1FHL sources. The four histograms report the significances for all 1FHL sources (All); 1FHL sources whose locations match 2FGL sources (2FGL); 1FHL extended sources that do not match 2FGL sources, but are less than 0.3 from 2FGL sources (non-2FGL_a); 1FHL point sources which do not match 2FGL sources (non-2FGL_b).

(A color version of this figure is available in the online journal.)

Figure 14 reports the distributions of flux and index for the 1FHL sources that are not in 2FGL, grouped as in Figure 13. The group non-2FGL_b has the lowest fluxes and smallest indices. In particular, this group hosts the four sources with the smallest indices (Γ < 1): 1FHL J1314.9−4241 (associated with the blazar MS 13121−4221), 1FHL J1856.9+0252 (associated with the presumed PWN HESS J1857+026), and 1FHL J2159.1−3344 and 1FHL J0432.2+5555 (not associated with any known sources). All these sources are very weak and have hard spectra in the > 10 GeV energy range.

Figure 15 shows the distribution on the sky of the 63 1FHL sources without 2FGL counterparts. Apart from the 9 extended sources from Table 6 (4 SNRs, 2 PWNe, and 3 sources without associations), most sources are located outside the Galactic plane: 9 blazars, 8 blazar candidates, and a large fraction of the 36 unassociated sources.

We conclude that most of the new γ-ray sources reported in the 1FHL catalog (not reported previously in the 2FGL catalog)

[89] Out of the 63 sources, 11 are associated with 1FGL sources that did not reach a TS value of 25 in the 2FGL analysis, which used 2 yr of LAT data.

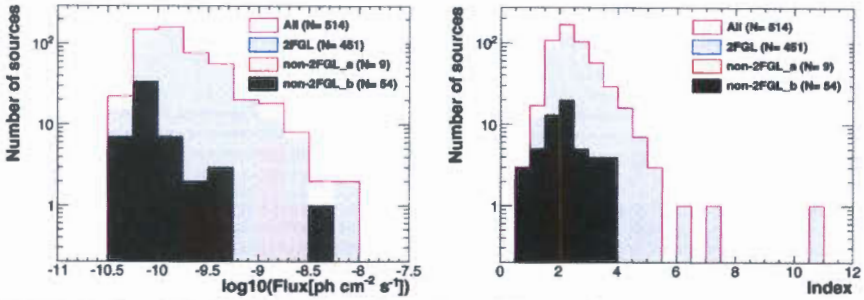

Figure 14. Distribution of the measured photon fluxes (left) and photon index (right) for the 1FHL sources. The four histograms report the significances for all 1FHL sources (All); 1FHL sources whose locations match any in the 2FGL catalog (2FGL); 1FHL extended sources which do not match any in the 2FGL, but are less than 0.3 from 2FGL sources (non-2FGL_a); 1FHL point sources that do not have corresponding 2FGL sources (non-2FGL_b).

(A color version of this figure is available in the online journal.)

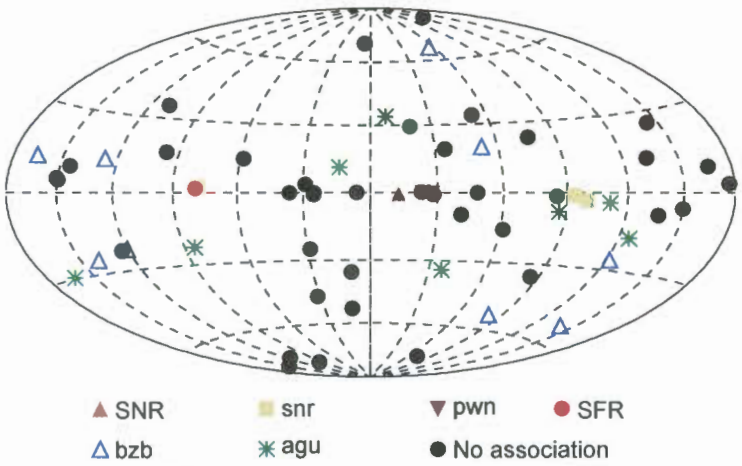

Figure 15. Sky map showing the locations of the 1FHL sources that do not have counterparts in the 2FGL catalog (groups non-2FGL_a and non-2FGL_b). The sources are depicted with the source classes described in Table 4. The projection is Hammer–Aitoff in Galactic coordinates.

(A color version of this figure is available in the online journal.)

are likely to be blazars with weak, hard-spectrum emission that might have been more active in the third year. As reported in Section 3.3, only two non-2FGL sources (1FHL J0318.8+2134 and 1FHL J1532.6−1317) have significantly greater average fluxes in the third year of LAT observations than they did during the first 2 yr (the time interval for the 2FGL catalog). The limited counting statistics above 10 GeV, however, make variability hard to confirm.

4.4. The 1FHL AGNs

The 1FHL catalog is strongly dominated by AGNs, with 393[90] sources associated with AGNs. Among them, blazar and blazar candidates[91] represent 86% of the sources that have associations. In this section we report on the overall γ-ray properties of these AGNs.

As for the 2FGL catalog, most of the extragalactic 1FHL sources are non-thermal-dominated or jet-dominated sources; that is, the broad-band emission is produced by high-energy particles accelerated in the magnetized jet of material ejected from the central engine. Non-thermal AGNs are classified by the frequency of the peak of the synchrotron emission, which is related to the maximum energy of the accelerated electrons. Here we used the convention proposed by Abdo et al. (2010a) and classify the AGNs as low-synchrotron-peaked (LSP), intermediate-synchrotron-peaked (ISP), and high-synchrotron-peaked (HSP) if the peak of the synchrotron emission $\nu_{syn_{peak}}$ is located below 10^{14} Hz, in the range 10^{14}–10^{15} Hz, or above 10^{15} Hz, respectively. This is commonly designated as the spectral energy distribution (SED) classification, and it is complementary to the broadly used optical classification, which uses the presence/absence of emission lines to classify sources as FSRQ or BL Lac-type.

Table 7 reports the optical and SED classifications, as well as the redshifts (if available) and the measured variability for

[90] The only non-AGN extragalactic source is the LMC.
[91] Most of the "agu" sources are expected to be blazars.

Table 7
Characteristics of the 1FHL Sources With AGN Associations

1FHL Name	R.A.	Decl.	Assoc.	Optical Class.	SED Class.	Redshift	Variability_BayesBlocks
J0007.7+4709	1.947	47.155	MG4 J000800+4712	BL Lac	LSP	0.28 & 2.1	1
J0008.7−2340	2.194	−23.674	RBS 0016	BL Lac	...	0.147	1
J0009.2+5032	2.316	50.541	NVSS J000922+503028	BL Lac	...	...	1
J0018.6+2946	4.673	29.776	RBS 0042	BL Lac	HSP	...	1
J0022.2−1853	5.555	−18.899	1RXS J002209.2−185333	BL Lac	HSP	...	1
J0022.5+0607	5.643	6.124	PKS 0019+058	BL Lac	LSP	...	1
J0033.6−1921	8.407	−19.361	KUV 00311−1938	BL Lac	HSP	0.610	1
J0035.2+1514	8.806	15.234	RX J0035.2+1515	BL Lac	HSP	...	1
J0035.9+5950	8.990	59.838	1ES 0033+595	BL Lac	HSP	...	1
J0037.8+1238	9.473	12.645	NVSS J003750+123818	BL Lac	HSP	0.089	1
J0040.3+4049	10.096	40.827	1ES 0037+405	BL Lac	HSP	...	1
J0043.7+3425	10.936	34.429	GB6 J0043+3426	FSRQ	...	0.966	1

Notes. This table is also available as a FITS file from the FSSC. R.A. and Decl. are celestial coordinates in J2000 epoch, Assoc. is the name of the associated (or identified) source counterpart, Optical Class. is the optical classification of the AGN, SED class is the SED classification (whenever available), and Variability_BayesBlocks is the number of Bayesian Blocks (see Section 3.3). Four of the sources have two distinct redshifts reported in the literature and their redshifts are listed here separated by the symbol "&." Three sources have redshifts in the literature that violate the spectroscopic lower limits reported in Shaw et al. (2013); these are listed as "z1 & LowLimit z2." Three 1FHL sources have double associations, the two distinct associated source names and characteristics are reported separated by the symbol "&."

(This table is available in its entirety in a machine-readable form in the online journal. A portion is shown here for guidance regarding its form and content.)

Table 8
Summary of SED Classifications and Available Redshifts for 1FHL Sources With AGN Associations

SED Classification	Number of Sources	Number with Measured Redshift (fraction)
HSP	162	76 (47%)
ISP	61	28 (46%)
LSP	99	75 (76%)
Not Classified	71	29 (41%)
Total	393	208 (53%)

all of the 1FHL AGN sources. The variability is quantified as described in Section 3.3, with the most variable sources having the highest number of blocks, and the sources with no significant variability having only one block. The optical and SED classifications, and redshifts, were obtained primarily from the 2LAC paper (Ackermann et al. 2011b), with the information for the non-2FGL AGNs being obtained from the BZCAT (Massaro et al. 2009). Moreover, we also used the recent work by Shaw et al. (2013) to obtain the optical classification and redshift information for some sources. We noted that seven AGNs with 1FHL associations have redshifts reported by Ackermann et al. (2011b) that are in conflict with the information reported by Shaw et al. (2013). For four sources (1FHL J0007.7+4709, 1FHL J0508.1+6737, 1FHL J1312.2−2158, and 1FHL J2116.2+3339) the newly reported redshifts by Shaw et al. (2013) do not match those of Ackermann et al. (2011b). For three others (1FHL J0909.3+2312, 1FHL J2016.3−0907, and 1FHL J2323.8+4210), the values given by Ackermann et al. (2011b) violate lower limits reported by Shaw et al. (2013). We report both values (or value and lower limit) in Table 7 as "z1 & z2" ("z1 & LowLimit z2"), where the first entry is retrieved from Ackermann et al. (2011b) and the second one (value or lower limit) from Shaw et al. (2013).

Table 8 summarizes the number of 1FHL AGN sources belonging to the various SED classifications with and without redshift determinations. Among all blazars, the dominant SED class is HSP, which makes up ~41% of the 1FHL AGNs. This is not a surprising result because HSPs typically have a hard spectrum (power-law index Γ 2) and hence they are expected to be the AGN source class that emit the highest-energy photons. Table 8 also shows that the 1FHL catalog has 208 (~53%) sources associated with AGNs of known redshifts,[92] from which the fractions of sources with measured redshifts are 47%, 46% and 41% for HSP, ISP, and sources without SED classification, respectively, and 76% for the LSP class. The fraction of LSPs with available redshifts is larger because 58 of the 99 LSPs are actually FSRQs which, by definition, have measured redshifts, while no ISP or HSP are FSRQs and the FSRQ optical classification overlaps exclusively with the LSP SED classification.

Figure 16 shows the distribution of the measured power-law indices of the 1FHL blazars in the energy ranges 100 MeV to 100 GeV (extracted from the 2FGL catalog table) and 10–500 GeV (from Table 3). The figure does not show the nine 1FHL sources that are associated with the five radio galaxies and the other four non-blazar AGNs. Note that the number of entries in the distributions from the left panel is less than that in the distributions in the right panel. This is because the 1FHL catalog contains 17 AGN associations (9 BL Lac objects and 8 blazar candidates) that do not exist in the 2FGL catalog (Section 4.3). The figure shows a clear spectral softening for each source class when the minimum energy is increased from 100 MeV to 10 GeV. This is due both to intrinsic softening of the spectra of many sources[93] and to γ-ray attenuation in the

[92] This number does not include the seven sources with conflicting redshift information reported above.

[93] The intrinsic softening can occur because of internal $\gamma\gamma$ absorption, which is energy dependent, or because of a steep decrease with energy of the number of high-energy particles (presumedly electrons/positrons) that are responsible for the high-energy γ rays.

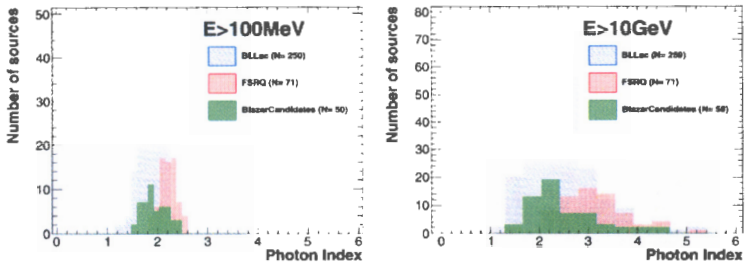

Figure 16. Distribution of measured photon index for selected groups of 1FHL AGN sources above 100 MeV (left: extracted from the 2FGL catalog) and above 10 GeV (right: extracted from Table 3). The three histograms show the distributions for three different groups of AGN associations: BL Lac objects, FSRQs, and AGU or blazar candidates. See text for further details.

(A color version of this figure is available in the online journal.)

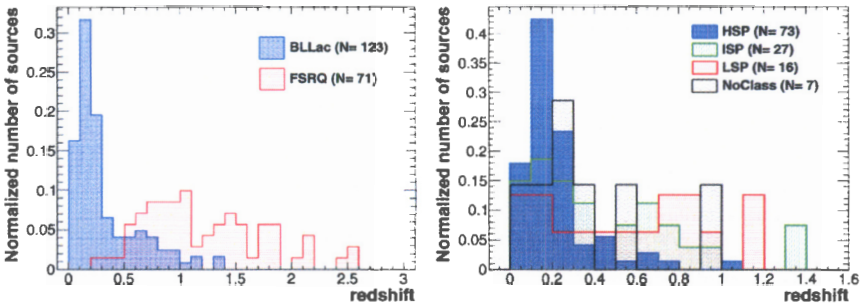

Figure 17. Distribution of redshifts for selected groups of 1FHL AGN sources. The left panel shows the normalized redshift distributions for BL Lac objects (blue dotted-filled, 123 sources) and FSRQs (red horizontal-line-filled, 71 sources). The right panel shows the normalized distributions for BL Lac objects classified as HSP (blue dotted-filled, 73 sources), ISP (green vertical-line-filled, 27 sources), LSP (red horizontal-line-filled, 16 sources) and sources without SED classification (black wavy-line-filled, 7 sources).

(A color version of this figure is available in the online journal.)

optical/UV EBL for distant ($z > 0.5$) sources. We also note that in both panels the photon indices of the FSRQs cluster at the largest index values, while BL Lac objects have the smallest index values. So even when the spectra are characterized using photons above 10 GeV, we find that about 30% of the BL Lac objects (77 out of 259) have indices harder than 2. The index distribution of the blazar candidates ("agu" sources) is similar to that of BL Lac objects, which suggests that a large fraction of these blazar candidates are actually BL Lac objects.

Figure 17 shows the redshift distribution for the BL Lac objects and FSRQs from the 1FHL catalog. For simplicity, we did not include in this plot the redshift distribution of the five radio galaxies, which cluster at low redshifts. Neither did we include the redshift distribution for the nine blazar candidates ("agu"), which span $z = 0$–1. We note that most of the BL Lac objects have redshifts less than 0.5, while most of the FSRQs have redshifts greater than 0.5. The lack of BL Lac objects at high redshift could be due to the different characteristics of BL Lac objects relative to FSRQs, which are known to have a stronger intrinsic γ-ray brightness (Abdo et al. 2010a). However, we also note that the observed redshift distribution of BL Lac objects has an important bias due to the difficulty of measuring their redshifts. About half the BL Lac objects associated with 1FHL sources do not have known redshifts, while all of the FSRQ associations have measured redshifts.

The right-hand panel in Figure 17 shows the redshift distribution for BL Lac objects split into the various SED classifications, namely HSP, ISP, and LSP. The figure also depicts the redshift distribution for the seven sources without SED classifications. The figure shows clearly that the distribution of HSPs (those with the highest synchrotron peak frequency) peaks at the lowest redshifts. We note that the above-mentioned trends, as well as the overall shape of the redshift distributions for BL Lac objects and FSRQs and for the different subclasses of BL Lac objects, are very similar to those shown in Figure 12 of the 2LAC paper (Ackermann et al. 2011b), hence indicating that selecting sources emitting above 10 GeV does not introduce any bias/distortion in the redshift properties of the sample of blazars detected by Fermi LAT.

Figure 18 shows a scatter plot of the photon index ($E > 100$ MeV and $E > 10$ GeV) versus the redshift for the various blazar subclasses: FSRQs, HSP-BL Lac objects, ISP-BL Lac objects, LSP-BL Lac objects and BL Lac objects without SED classification. There is no redshift evolution in the spectral shape characterized with photon energies above 100 MeV, which is in agreement with the results reported in Figure 19 of the 2LAC paper.[94] However, the photon index computed with energies above 10 GeV has a redshift dependence: sources get softer with increasing redshift. This trend is not apparent in the BL Lac sample, which clusters at relatively low redshifts (mostly below 0.5); but it is noticeable in the sample of FSRQs, which

[94] The data used to produced the left panel from Figure 18 are the same as used in the 2LAC, differing only in the selection of the blazar sample: only 194 1FHL blazars (FSRQs+BL Lac objects) are being used here.

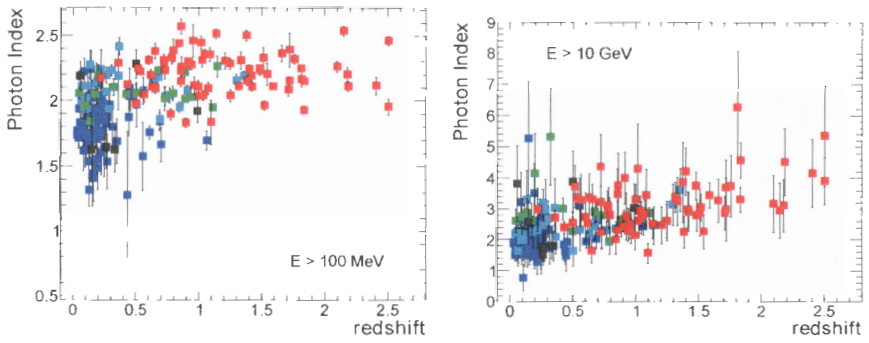

Figure 18. Power-law index from the observed source spectra vs. redshift for the 1FHL sources with available redshifts. The left panel shows the power-law index describing the spectral shape above 100 MeV (extracted from the 2FGL catalog) and the right panel shows the power-law index describing the spectral shape above 10 GeV (this work). In both panels, red indicates FSRQs (71 sources), dark-blue for HSP-BL Lac objects (73), light-blue for ISP-BL Lac objects (27), green for LSP-BL Lac objects (16), and black for BL Lac objects with unclassified SEDs (7).

extends up to redshift 2.5. A potential reason for this evolution of the > 10 GeV spectral shape (but not for the > 100 MeV spectral shape) is the attenuation of the γ rays on optical/UV photons of the EBL, which is energy dependent and affects photons only above a few tens of GeV. A cosmological evolution of the FSRQ sample that introduces an intrinsic softening of the spectra may also play a role. However, for consistency with the experimental observations reported in Figure 18, such a cosmological evolution of FSRQs should affect only the emission above 10 GeV.

The last column of Table 7 quantifies the variability of the 1FHL sources, determined as described in Section 3.3. Among the 43 1FHL AGN sources identified as variable we find 22 LSPs (22% of the 99 1FHL LSP associations), 7 ISPs (13% of the 61 1FHL ISP associations), 6 HSPs (4% of the 162 1FHL HSP sources), and 8 sources with no SED classifications (11% of the 71 1FHL sources with unclassified SEDs). One of the outstanding characteristics is that most of the 1FHL sources identified as variable belong to the blazar subclass LSP, not to the subclass HSP, which is the dominant blazar subclass, and which has a larger number of high-energy photons. We stress that the three classic VHE blazars most variable above a few hundred GeV, namely Mrk 421, Mrk 501 and PKS 2155−304, are not found to be variable in the 1FHL catalog. This is surprising, given that these three also have the largest numbers of detected photons above 10 GeV: 432, 247, and 132, respectively (as evaluated from the likelihood analysis). Moreover, the fraction of 1FHL LSPs identified as variable (~22%) is substantially higher than the fraction of 1FHL HSPs identified as variable (~4%). This trend was already observed in the 2FGL blazars at energies above 100 MeV, and reported in the 2LAC paper (e.g., see Figures 26 and 27 of that work). Therefore, we can confirm that, across the entire energy range of the LAT, the LSPs are more variable than the HSPs. These experimental observations show that the variability in the falling segment of the high-energy (inverse Compton) SED bump is greater than that in the rising segment of the SED bump.

4.5. Pulsars above 10 GeV

Pulsars are the second-largest class of associated sources in the 1FHL catalog. The detection with IACTs of pulsations from the Crab, first at > 25 GeV (Aliu et al. 2008), and more recently at VHE (VERITAS Collaboration et al. 2011; Aleksić et al. 2012b) makes the study of high-energy (> 10 GeV) emission from γ-ray pulsars with the LAT especially timely. A similar study conducted on EGRET data above 10 GeV revealed 37 events coincident with five γ-ray pulsars (Thompson et al. 2005).

The second Fermi LAT catalog of γ-ray pulsars (Abdo et al. 2013; hereafter referred to as 2PC), includes results for 117 γ-ray pulsars detected in 3 yr of LAT data. In this section we focus on pulsar emission above 10 GeV.

Pulsars are naturally associated with SNRs and PWNs, both of which also can be bright VHE emitters. In addition to knowing how many pulsars are associated with 1FHL sources, we would also like to determine which of these pulsars can be identified with the 1FHL sources, by showing pulsations above 10 GeV (HPSR).

The pulsation analysis described here relies on the 2PC pulsar timing models.[95] In addition to studying 1FHL sources associated with pulsars, the analysis was extended to include a number of 2PC pulsars that are candidate HPSRs, despite having no associated 1FHL source. Out of the 27 pulsars associated with 1FHL sources (listed in Table 9), two (PSRs J1536−4948 and J2339−0533) are not included in 2PC and are therefore left out of this analysis.

In order to test for high-energy pulsations we used a likelihood ratio test, comparing the distribution in pulsar phase of the high-energy events with the low-energy pulse profile. We considered the standard H-test (de Jager et al. 1989) but found it to be less sensitive. This is not too surprising, given that the H-test involves no assumptions about the pulse profile[96] while the likelihood ratio test benefits from the available information on the low-energy pulse profile, even if this may not necessarily be exactly the same as the high-energy profile. We used high-energy (> 10 GeV) photons within an RoI of 0.6 radius for front-converting (Front) events and 1.2 for back-converting (Back) events, roughly corresponding to the 95% containment angles of the reconstructed incoming photon direction for

[95] Available at http://fermi.gsfc.nasa.gov/ssc/data/access/lat/ephems/.
[96] Its usage is generally recommended in cases such as the standard LAT searches for γ-ray pulsars, for which there is no a priori knowledge about the shape of the γ-ray light curve.

Table 9
1FHL Sources Associated with Fermi-LAT Pulsars

1FHL	PSR	P (ms)	l (deg)	b (deg)	n_{10}	P_{10}	n_{25}	P_{25}	Ref.
J0007.3+7303	J0007+7303[c]	316	119.7	+10.5	179	$< 2 \times 10^{-9}$	20	1.7×10^{-3}	(1, 2, 3)
J0205.7+6449	J0205+6449	65.7	130.7	+3.1	38	> 0.05	12	> 0.05	(4)
J0534.5+2201	J0534+2200[†,c]	33.6	184.6	−5.8	674	6.3×10^{-8}	191	2.4×10^{-2}	Crab (5, 6, 7)
J0614.0−3325	J0614−3329	3.15	240.5	−21.8	26	$< 2 \times 10^{-9}$	3	2.0×10^{-2}	(8)
J0633.9+1746	J0633+1746[c]	237	195.1	+4.3	260	$< 2 \times 10^{-9}$	11	1.4×10^{-5}	Geminga (9)
J0835.3−4510	J0835−4510[†,c]	89.4	263.6	−2.8	1005	$< 2 \times 10^{-9}$	56	$< 2 \times 10^{-9}$	Vela (10, 11)
J1022.6−5745	J1023−5746	112	284.2	−0.4	152	> 0.05	46	> 0.05	(12)
J1028.4−5819	J1028−5819[c]	91.4	285.1	−0.5	164	$< 2 \times 10^{-9}$	41	4.0×10^{-2}	(13)
J1048.4−5832	J1048−5832	124	287.4	+0.6	85	9.7×10^{-6}	22	2.1×10^{-2}	(14)
J1112.5−6105	J1112−6103	65.0	291.2	−0.5	112	> 0.05	28	> 0.05	
J1231.2−1414	J1231−1411	3.68	295.5	+48.4	15	5.3×10^{-7}	4	> 0.05	(8)
J1413.4−6205	J1413−6205	110	312.4	−0.7	278	4.4×10^{-3}	64	1.5×10^{-2}	(12)
J1418.6−6059	J1418−6058	111	313.3	+0.1	324	> 0.05	72	> 0.05	(2)
J1420.1−6047	J1420−6048	68.2	313.5	+0.2	278	> 0.05	65	> 0.05	(15)
J1514.3−4945	J1514−4946	3.58	325.2	+6.8	24	1.7×10^{-4}	3	> 0.05	(16)
J1536.4−4951	J1536−4948	3.08	328.2	+4.8	...	...	...	...	Not in 2PC
J1620.7−4928	J1620−4927	172	333.9	+0.4	297	9.4×10^{-3}	77	> 0.05	(17)
J1709.7−4429	J1709−4429[c]	103	343.1	−2.7	272	$< 2 \times 10^{-9}$	25	> 0.05	(18)
J1809.8−2329	J1809−2332	147	7.4	−2.0	119	$< 2 \times 10^{-9}$	18	4.3×10^{-2}	(2)
J1836.4+5925	J1836+5925	173	88.9	+25.0	36	1.0×10^{-4}	2	1.0×10^{-2}*	(2, 19)
J1907.7+0600	J1907+0602[c]	107	40.2	−0.9	158	2.3×10^{-4}	36	> 0.05	(2, 20, 21)
J1953.3+3251	J1952+3252	39.5	68.8	+2.8	48	1.2×10^{-5}	7	> 0.05	(18)
J1958.6+2845	J1958+2846	290	65.9	−0.4	64	1.0×10^{-2}	11	> 0.05	(2)
J2021.0+3651	J2021+3651[c]	104	75.2	+0.1	107	$< 2 \times 10^{-9}$	20	7.6×10^{-3}	(21, 22, 23)
J2032.1+4125	J2032+4127[c]	143	80.2	+1.0	210	5.6×10^{-8}	54	> 0.05	(2, 24)
J2229.0+6114	J2229+6114[c]	51.6	106.7	+3.0	86	$< 2 \times 10^{-9}$	14	6.1×10^{-3}	(14, 25)
J2339.8−0530	J2339−0533	2.88	81.1	−62.4	...	...	...	...	Not in 2PC

Notes. 1FHL source; associated pulsar (in bold if seen at > 25 GeV); a [†] (^c) implies a LAT-detected (TeV-detected) PWN; P is the pulsar period, in milliseconds, Galactic longitude (l) and latitude (b) in degrees; n_{10} (n_{25}) is the number of > 10 (25) GeV photons (within a 95% containment radius) and P_{10} (P_{25}) the corresponding tail probability. We quote only p-values < 0.05 and > 2×10^{-9} (~6σ). (*) For PSR J1836+5925, the two > 25 GeV events result in a p-value = 5.52×10^{-2} according to the asymptotic approximation, but Monte Carlo simulations show that the true p-value is 1.0×10^{-2}, so the pulsations can be considered significant.

References. (1) Abdo et al. 2008; (2) Abdo et al. 2009b; (3) Aliu et al. 2013; (4) Abdo et al. 2009c; (5) Abdo et al. 2010g; (6) Aliu et al. 2008; (7) VERITAS Collaboration et al. 2011; (8) Ransom et al. 2011; (9) Abdo et al. 2010j; (10) Abdo et al. 2009h; (11) Abdo et al. 2010q; (12) Saz Parkinson et al. 2010; (13) Abdo et al. 2009g; (14) Abdo et al. 2009d; (15) Weltevrede et al. 2010; (16) Kerr et al. 2012; (17) Pletsch et al. 2012a; (18) Abdo et al. 2010r; (19) Abdo et al. 2010f; (20) Abdo et al. (2010n); (21) Abdo et al. 2009i; (22) Halpern et al. 2008; (23) Abdo et al. 2009f; (24) Camilo et al. 2009; (25) Acciari et al. 2009.

normal incidence above 10 GeV. For the low-energy profile, we assumed the probability distribution function (PDF), with phase φ, obtained in the 2PC using the weighted LAT photons above 100 MeV (where the weight of each photon corresponds to the probability that it comes from the pulsar; see 2PC for details):

$$\mathrm{PDF}_{\mathrm{LE}}(\varphi) = d + \sum_{i=1}^{n} c_i \cdot f_i(\varphi), \quad (1)$$

a combination of n skewed Gaussian and Lorentzian distributions f_i. The overall normalization of the PDF is defined such that $d + \sum_{i=1}^{n} c_i = 1$, where d represents the unpulsed (or "DC") component of the pulsar. For the high-energy PDF, we considered the family of distributions given by:

$$\mathrm{PDF}_{\mathrm{HE}}(\varphi) = (1 - x) + x \cdot \frac{\mathrm{PDF}_{\mathrm{LE}}(\varphi) - d}{1 - d} \quad (2)$$

with $0 \leq x \leq 1$. We maximized a likelihood function derived from $\mathrm{PDF}_{\mathrm{HE}}$ with respect to x, to give $L(\hat{x})$, and compared it to the null hypothesis, for $x = 0$, that there is no pulsation, i.e., $\mathrm{PDF}_{\mathrm{HE}}(\varphi) = 1$. By construction, the likelihood under the null hypothesis is $L(0) = 1$, so the test statistic, defined as $TS = -2\ln(L(0)/L(\hat{x}))$, can be simplified to $TS = 2\ln L(\hat{x})$.

We converted the measured value of TS into a tail probability (or p-value, P) by assuming (by virtue of Wilks' theorem) that the TS follows a χ^2 distribution with 1 degree of freedom. Since we are only testing for a positive correlation (one-sided test) between the low and high energy pulse profiles (whereas a negative correlation is equally likely in the null hypothesis), we divide the (two-sided) p-values by 2. We set a threshold of $P = 0.05$ to claim evidence for pulsations, with P_{10} representing the p-value obtained using > 10 GeV events and P_{25} corresponding to the p-value obtained using > 25 GeV events. Given that we are using an asymptotic approximation to convert between the measured TS values and the corresponding p-values, we report only p-values greater than 2.0×10^{-9} (~6σ); rather than provide unreliable numbers in the tails of the distribution, we prefer to quote the rest only as upper limits.

We validated the procedure with Monte Carlo simulations. Given a high-energy profile with a certain number of events, n, we generated random sets of n phases uniformly distributed between 0 and 1. We then performed exactly the same test on these fake data sets and measured the rate of false positives. We repeated the simulations for every pulse profile and verified that the asymptotic distribution is valid in all cases with more than 2 events.

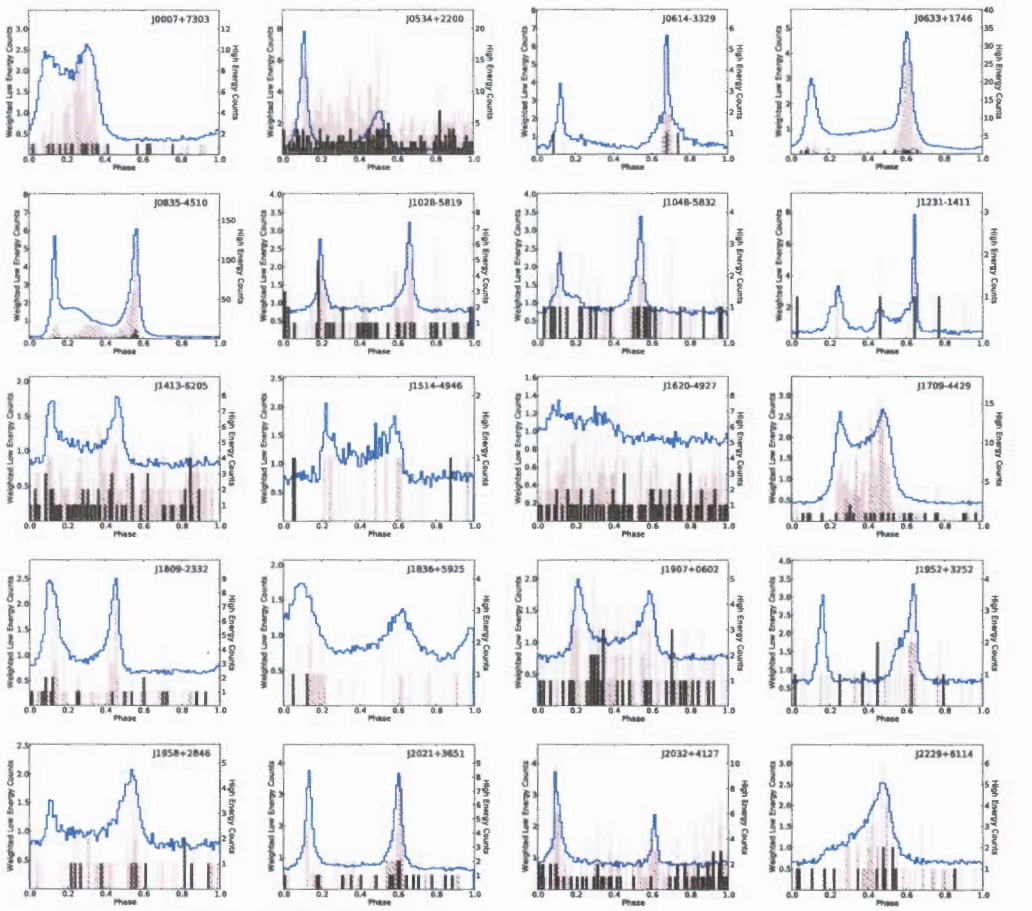

Figure 19. Folded pulse profiles of γ-ray pulsars associated with 1FHL sources, obtained with 3 yr of P7CLEAN Fermi-LAT data. The blue histogram (y-axis scale on the left) represents the weighted "low energy" (> 100 MeV) light curve (using the 2PC spectral model). The filled histograms (y-axis scale on the right) show the events above 10 GeV (pink) and 25 GeV (black).

(A color version of this figure is available in the online journal.)

In the case of J1836+5925, only two events are detected above 25 GeV. Although the asymptotic approximation fails to reveal significant pulsations ($P = 5.5 \times 10^{-2}$, above the significance threshold of 0.05), the Monte Carlo simulations demonstrate that the false positive rate is actually 1.0×10^{-2}, so the > 25 GeV pulsations, in fact, pass the threshold. Table 9 summarizes the results of the pulsation analysis. Out of the 25 γ-ray pulsars associated with 1FHL sources for which the pulsation analysis was performed, 20 show evidence for pulsations above 10 GeV ($P_{10} < 0.05$) and 12 of these (listed in bold in Table 9) show evidence for pulsations above 25 GeV ($P_{25} < 0.05$). Figure 19 shows the pulse profiles of these 20 pulsars, including the weighted low-energy (> 100 MeV) pulse profile, along with the folded > 10 GeV and > 25 GeV photons.

Five γ-ray pulsars associated with 1FHL sources show no pulsations above 10 GeV:

1. PSR J0205+6449, associated with the SNR 3C 58, is thought to be one of the youngest pulsars in the Galaxy and is shown in 2PC to have a GeV PWN.
2. PSR J1023−5746 is coincident with HESS J1023−575 and is identified as a promising GeV PWN candidate (e.g., Saz Parkinson et al. 2010; Ackermann et al. 2011c).
3. PSR J1112−6103 is identified in 2PC as having significant extended off-peak emission.
4. PSR J1418−6058 in the Kookaburra complex is coincident with the Rabbit PWN and thought to be powering the PWN candidate HESS J1418−609.

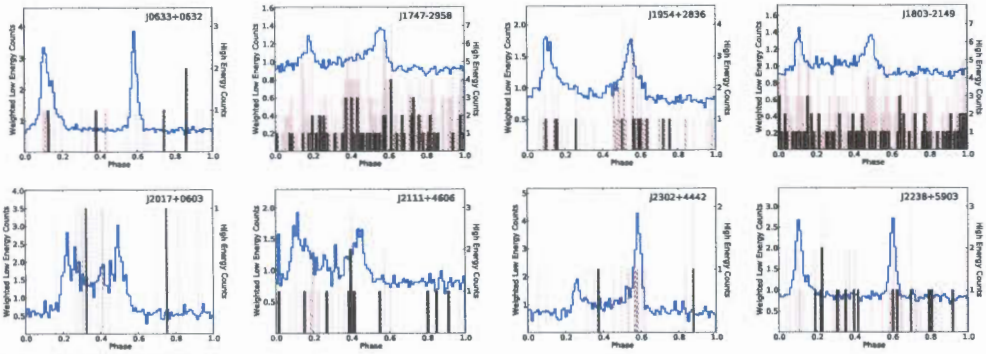

Figure 20. Folded pulse profiles of γ -ray pulsars with no corresponding 1FHL sources, obtained with 3 yr of P7CLEAN Fermi-LAT data. The blue histogram (y-axis scale on the left) represents the weighted "low energy" (> 100 MeV) light curve (using the 2PC spectral model). The filled histograms (y-axis scale on the right) show the events above 10 GeV (pink) and 25 GeV (black).

(A color version of this figure is available in the online journal.)

Table 10
Fermi-LAT γ -Ray Pulsars with Hints of > 10 GeV Emission but No 1FHL Association

PSR	P (ms)	l (deg)	b (deg)	n_{10}	P_{10}	n_{25}	P_{25}	Ref.
J0218+4232	2.32	139.5	−17.5	79	> 0.05	23	> 0.05	(1)
J0633+0632	297	205.1	−0.9	24	1.3×10^{-2}	5	> 0.05	(2)
J1509−5850	88.9	320.0	−0.6	187	> 0.05	52	> 0.05	(3)
J1747−2958	98.8	359.3	−0.8	272	3.8×10^{-2}	64	> 0.05	
J1803−2149#	106	8.1	+0.2	270	1.4×10^{-2}	76	> 0.05	(4)
J1826−1256	110	18.6	−0.4	304	> 0.05	80	> 0.05	(2)
J1838−0537	146	26.5	+0.2	321	> 0.05	96	> 0.05	(5)
J1954+2836	92.7	65.2	+0.4	66	4.8×10^{-6}	12	6.5×10^{-3}	(6, 7, 8)
J2017+0603	2.90	48.6	−16.0	16	1.4×10^{-2}	2	> 0.05	(9)
J2021+4026	265	78.2	+2.1	289	> 0.05	77	> 0.05	(2)
J2043+1711	2.38	61.9	−15.3	0	> 0.05	0	> 0.05	(10)
J2111+4606	158	88.3	−1.5	33	3.4×10^{-3}	11	> 0.05	(4)
J2238+5903	163	106.6	+0.5	51	4.0×10^{-2}	14	> 0.05	(2)
J2302+4442	5.20	103.4	−14.0	19	5.1×10^{-4}	2	> 0.05	(9)

Notes. PSR is the name of γ -ray pulsar (in bold when detected above 25 GeV). A † next to the name means a GeV PWN is detected by the LAT, while a # means a TeV (> 100 GeV) PWN is detected by ground-based instruments (see http://tevcat.uchicago.edu); P is the pulsar period, in milliseconds; The Galactic longitude (l) and latitude (b), are given in degrees. n_{10} (n_{25}) is the number of photons (within the 95% containment radius of the PSF) above 10 (25) GeV and P_{10} (P_{25}) gives the corresponding tail probabilities, against a null hypothesis of no pulsations. We quote only p-values < 0.05 and > 2×10^{-9} (~6σ).

References. (1) Abdo et al. 2009a; (2) Abdo et al. 2009b; (3) Weltevrede et al. 2010; (4) Pletsch et al. 2012a; (5) Pletsch et al. 2012b; (6) Saz Parkinson et al. 2010; (7) Abdo et al. 2009f; (8) Aleksić et al. 2010; (9) Cognard et al. 2011; (10) Guillemot et al. 2012.

5. PSR J1420−6048, also in the Kookaburra complex, is in the vicinity of HESS J1420−607 and is a promising LAT PWN candidate (Acero et al. 2013).

In short, the > 10 GeV emission from these five 1FHL sources is more likely to be from PWNs than from the pulsars themselves.

Because a pulsation search is more sensitive than a simple source detection search, we extended the analysis to include pulsars from 2PC whose spectra show possible emission above 10 GeV, even if they have no associated 1FHL source. There are 14 additional pulsars in 2PC with at least one spectral bin above 10 GeV detected with TS □ 4, a ~2σ detection.[97] The results of the pulsation analysis for these pulsars are listed in Table 10. Eight out of the 14 pulsars selected in this way show evidence for pulsations above 10 GeV, and one of them (J1954+2836) shows evidence for pulsations even above 25 GeV. The pulse profiles of these eight pulsars are shown in Figure 20.

The effect of the spectral cutoff in pulsars is manifested by the dramatic drop in photon statistics from 10 GeV to 25 GeV (cf. Columns 6 and 8 of Table 9 and Columns 5 and 7 of Table 10). A change in pulse profile at higher energies (> 10 GeV), compared to low energies (> 100 MeV), is also apparent, with the widths of the peaks typically narrowing and the height of the first peak decreasing in significance. These features of the high-energy profiles have been reported for the brightest γ -ray pulsars like Vela, the Crab, and Geminga (Abdo et al. 2009h, 2010g, 2010j), but we show here that they are present in other pulsars too,

[97] See Abdo et al. (2013) for further details, including plots, regarding the spectral analysis of these and other LAT pulsars.

Table 11
Fermi-LAT γ-Ray Pulsars Detected above 25 GeV

PSR	E_{max}	$E_{max}^{detected}$	$\Phi_{\gamma_{max}}$	Notes
J0007+7303*	28	788	0.64	
J0534+2200†*	26	784	0.33	Crab
J0614−3329	63	63.6	0.68	
J0633+1746*	33	52.7	0.05	Geminga
J0835−4510†*	37	752	0.28	Vela
J1028−5819	27	386	0.49	
J1048−5832	35	201	0.28	
J1413−6205	29	331	0.28	
J1809−2332	26	159	0.07	
J1836+5925	26	97.9	0.05	
J1954+2836	62	95.7	0.57	
J2021+3651*	26	113	0.64	
J2229+6114*	31	169	0.17	

Notes. PSR is the name of γ-ray pulsar, a † implies a GeV PWN is detected by the LAT, while a * implies an associated TeV PWN, detected by ground-based instruments above 100 GeV (see http://tevcat.uchicago.edu). E_{max} is the maximum energy (in GeV) above which $P < 0.05$ is still obtained while $E_{max}^{detected}$ is the highest-energy event detected (in GeV) and $\Phi_{\gamma_{max}}$ is the corresponding pulsar phase of this event.

including MSPs, like J0614−3329. In the case of the Crab, the LAT pulse profile shown in Figure 19 is heavily contaminated by the emission from the PWN. An analysis beyond the scope of this paper would be required to disentangle the two spectral components and provide a more sensitive analysis of the Crab pulsar in the > 10 GeV energy range. In the case of Vela, another feature that is apparent in the high-energy profile (see Figure 19) is an energy-dependent shift of the position of the third ("middle") peak, which moves toward the second peak with increasing energy, as reported by Abdo et al. (2009h). This change in profile at higher energies highlights a shortcoming of the analysis described here. The choice of the low-energy (> 100 MeV) pulse profile as a template for the pulsation search in the high-energy events was based in part on the assumption that the difference between the two profiles would be relatively modest.

Beyond 25 GeV, the drop in statistics for γ-ray pulsars becomes even more dramatic. Nevertheless, a number of pulsars in this study still have evidence of pulsations above 25 GeV. By scanning in energy (in steps of 1 GeV) we determined, for each pulsar, the energy beyond which the tail probability increases above 5%. Given the very small statistics, we relied on Monte Carlo simulations to obtain the p-values and corresponding energy thresholds. For the same reason, we caution against considering these as significant detections. Table 11 summarizes the results of this scan.

The presence of a PWN will complicate studies of pulsations at the highest energies. The high-energy γ-ray emission from PWNs can be particularly significant relative to the pulsars they are associated with, especially for some young, energetic pulsars (e.g., the Crab). An associated PWN can thus represent a significant background, limiting the sensitivity of a pulsation search. In the case of the Crab, the PWN is particularly bright, both at GeV and TeV energies. Thus, although the Crab pulsar has been detected (in fact, is the only pulsar detected) by IACTs above 100 GeV, the LAT results, shown in Table 9, are not as significant as those for a number of other > 25 GeV γ-ray pulsars. Indeed, with the current analysis, we are unable to detect pulsations beyond 26 GeV for the Crab. In Tables 9 and 10 we flag those with a LAT-detected GeV PWN or a TeV (> 100 GeV) PWN detected by IACTs. The maximum energy and phase columns of Table 11 suggest that we may be detecting events from a number of PWNs. For example, in the case of J0007+7303, the highest-energy event is 788 GeV, arriving at phase 0.64, far from the pulsar peaks, suggesting that a PWN origin is more likely than a PSR origin. VERITAS recently reported the detection of such a PWN above 100 GeV (Aliu et al. 2013).

The 28 HPSRs discussed in this section include members of every class of pulsar detected so far by the LAT and include the 5 brightest EGRET-detected pulsars[98]: 5 young (non-recycled) radio-loud γ-ray pulsars, 13 young (non-recycled) radio-quiet γ-ray pulsars, and 5 γ-ray MSPs. It is not obvious how to select the best candidates for the detection of pulsations at VHE with IACTs, since any such selection must depend on many assumptions, and spectral extrapolations from 10 GeV upward are notoriously unreliable. Improving the analysis for pulsations to address the shortcomings discussed above is left for future publications. A dedicated treatment of the separate PWN and PSR spectral components would likely improve the sensitivity of our search for pulsations, especially for those pulsars affected by a high level of PWN emission. Finally, a different choice of templates with which to compare the high-energy pulse profile (e.g., the > 1 GeV pulse profile), taking into account the evolution with energy of the pulse profile should also improve the sensitivity of the pulsation search. The sensitivity will, in any case, improve as the LAT data continue to accumulate.

5. GOOD CANDIDATES FOR VHE DETECTION

Astrophysical interest in γ rays extends beyond the energy range that is easily accessible to a space-based instrument like the Fermi LAT, which is limited by the size and mass of a satellite. Ground-based γ-ray telescopes that use Earth's atmosphere as a detector have enormous collecting areas and can operate successfully at energies where the LAT simply runs out of photons. Present and future VHE telescopes include both particle detector arrays (e.g., Tibet AS, ARGO-YBJ, HAWC and LHASSO) and IACTs, which are presently the most sensitive VHE instruments. The survey capability of the Fermi LAT at high energies provides a valuable complement to these IACTs, which are pointed instruments. It is worth noting that the 2FGL catalog of sources detected above 100 MeV has 1873 entries while the number of sources detected above 100 GeV and reported in TeVCat (version 3.400) is only 143 (including announced but not published VHE detections). Therefore, the LAT catalogs, and particularly this one above 10 GeV, offer candidate VHE targets. The 10 GeV minimum energy used for the 1FHL catalog analysis is a good compromise between having an adequate number of photons measured by LAT and being close to the energy range where IACTs operate. In this section we describe the best VHE candidates among the full set of the 1FHL catalog sources.

The most advanced IACTs are currently H.E.S.S. and VERITAS (arrays of four ~12 m telescopes; Hinton 2004; Weekes et al. 2002), and MAGIC (two telescopes of ~17 m diameter; Lorenz 2004). H.E.S.S. and VERITAS have energy thresholds[99] of ~100 GeV (and typically measure γ-ray

[98] PSR J1057−5226 (B1055−52) is the only EGRET pulsar not detected above 10 GeV.
[99] The energy threshold is conventionally defined as the peak in the differential energy trigger rate for a "Crab nebula-like" spectrum.

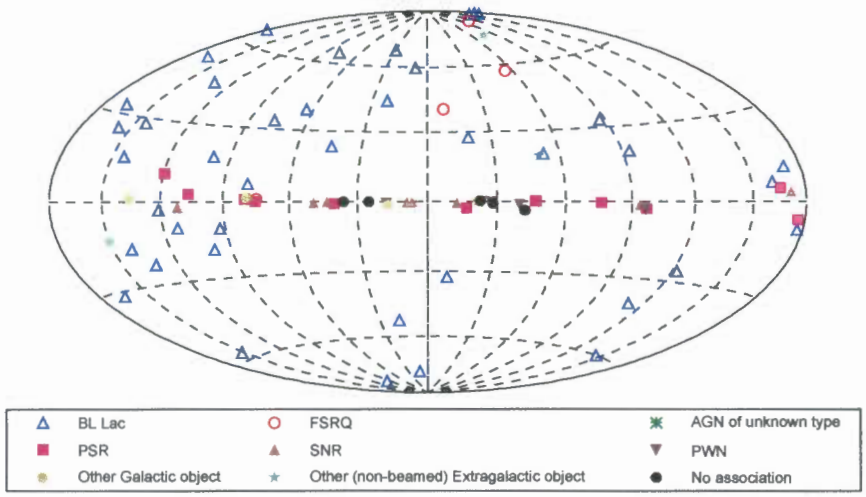

Figure 21. Sky map showing the 1FHL sources that have been detected at VHE by IACTs. The markers represent the source classes reported in Table 4. The projection is Hammer–Aitoff in Galactic coordinates.

(A color version of this figure is available in the online journal.)

spectra above 140 GeV) while MAGIC has an energy threshold of 60 GeV (and typically measures γ -ray spectra above 80 GeV). H.E.S.S added a 28 m diameter telescope to the existing array in Summer 2011. The resulting H.E.S.S II array has been operational since 2012 September and should allow the system to reduce the energy threshold below 50 GeV. The planned Cherenkov Telescope Array (CTA) will be even more powerful in terms of sensitivity and operational γ -ray energy range (Bernlöhr et al. 2013). The currently operating IACTs have effective fields of view of less than 4° degrees and so usually operate in a targeted observation mode. The photon fluxes in the VHE range are very low and hence relatively long observing times (□ 5–10 hr) are typically required to make detections. Because IACTs can operate only on clear, essentially moonless nights,[100] the duty cycles are typically only about 10%–12%, which corresponds to □ 1000 hr observing time annually. The Galactic plane is the only extended region that has been systematically scanned with the latest generation of IACTs.

The number of 1FHL sources that have associations with known VHE emitters is 84, which is about 2/3 of all the known VHE emitters. IACTs are responsible for the discovery of 81, while the other three were first detected in the VHE range by MILAGRO, a water Cherenkov detector (Atkins et al. 2004). These sources are depicted in Figure 21. We note that in the 2FGL catalog, coincidentally, 84 sources were associated with VHE emitters (not accounting for the association of 2FGL J2229.0+6114 with two VHE sources). In addition, 14 2FGL sources have been reported to be VHE emitters since the publication of the 2FGL catalog (see TeVCat). Therefore, of the 1873 sources in the 2FGL catalog, 98 now are associated with VHE sources, while of the 514 sources in the 1FHL, 84 have VHE counterparts. The VHE sources in common total 80. The 1FHL sources with VHE associations that are not in the 2FGL catalog are the blazars PKS 0548−322 and MS 13121−4221, the cocoon of freshly accelerated cosmic rays in the Cygnus X star-forming region (Ackermann et al. 2011a), and the unidentified source HESS J1857+026 (presumed to be a PWN; Klepser 2011). On the other hand, most of the 2FGL sources with VHE associations that are not in the 1FHL catalog are GeV pulsars that were associated with spatially extended, Galactic TeV sources. Only three point-like TeV sources with associations in the 2FGL catalog do not also have associations in the 1FHL catalog: the blazar 1ES 0414+009, and the starburst galaxies NGC 253 and M82. Each of these required very long exposures for VHE detection: ~70 hr with H.E.S.S. to detect the blazar and ~130 hr each with H.E.S.S. and VERITAS to detect the starburst galaxies.

This comparison shows that by limiting the energy range to > 10 GeV, the 1FHL sources do not miss many VHE sources. Naturally, among the 1FHL sources, some are more feasibly detectable at VHE. In the subsections below we describe the criteria that we used to select the most promising VHE source candidates among the 1FHL sources, and report the results.

5.1. Criteria for Selection of TeV candidates

Figure 22 shows the distribution of fluxes above 10 GeV (F_{10}) and above 50 GeV (F_{50}) for the 1FHL sources. The quantities F_{10} are directly provided by the likelihood analysis (Table 3), while the values of F_{50} are calculated from the power-law spectra. The figure shows that the known TeV sources cluster at the highest fluxes, this correlation being clearer for F_{50}. Such a relation is quite natural since the energy 50 GeV is close to the analysis energy threshold of the current generation of IACTs. Therefore, F_{50} is a very good indicator of the VHE flux.

Two additional quantities can also be used to select good candidates for VHE detection. These are the spectral index

[100] MAGIC can operate during nights with moderate moonlight with a reduced PMT HV, and VERITAS can operate even during bright moon by using an optical filter in front of the PMT camera. Such operation increases the energy threshold and reduces the sensitivity of the observations.

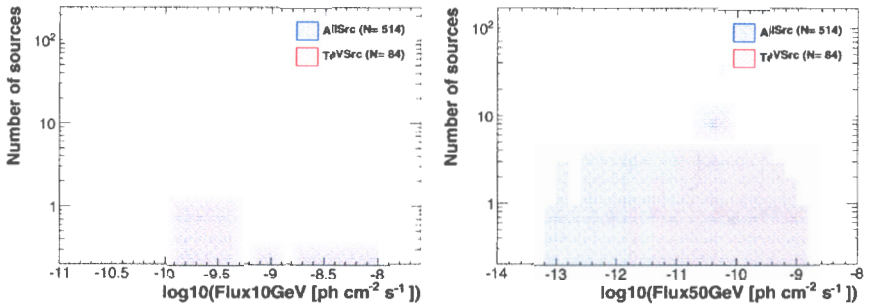

Figure 22. Distributions of measured flux above 10 GeV (left) and estimated flux above 50 GeV (right). The blue histograms depict all the 1FHL sources, while the red filled histograms show the 1FHL sources that have already been detected at VHE.

(A color version of this figure is available in the online journal.)

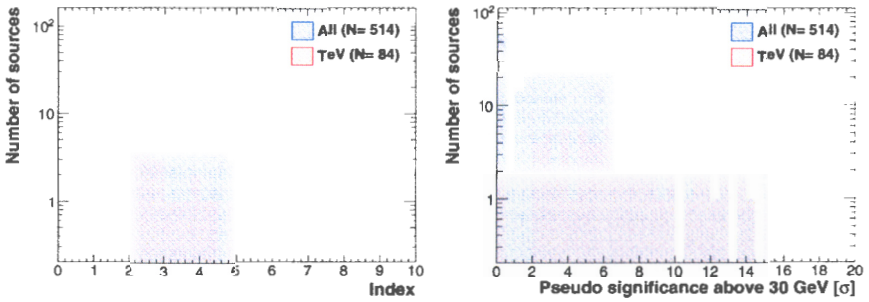

Figure 23. Distribution of the power-law index resulting from the spectral fits above 10 GeV (left) and the pseudo significance of the detection above 30 GeV (right, see text for definition). The blue histograms depict all the 1FHL sources, while the red filled histograms show the 1FHL sources that have already been detected at VHE.

(A color version of this figure is available in the online journal.)

above 10 GeV (Γ_{10}; see Table 3) and the pseudo significance of the signal above 30 GeV, Sig_{30}, which we define as $(TS_{30\_100} + TS_{100\_500})^{1/2}$, where TS_{30_100} and TS_{100_500} are TS values for the 30–100 GeV and 100–500 GeV energy bands, respectively, reported in the catalog data product. The distributions of these quantities for all the 1FHL sources are shown in Figure 23. The known VHE sources cluster at low Γ_{10} values and at high Sig_{30} values. Even though these quantities are not as powerful discriminators as F_{50}, they can help to remove from consideration sources that are not likely VHE emitters.

We adopted the following criteria to select 1FHL sources that have not been detected at VHE but have properties similar to those that have associations with known VHE sources: (1) $Sig_{30} > 3$; (2) $\Gamma_{10} < 3$; and (3) $F_{50} > 10^{-11}$ photons cm^{-2} s^{-1}.

As one can infer from Figures 22 and 23, the cut on F_{50} is the most restrictive, although the three cuts are strongly correlated. For instance, when applying the cuts in the order listed above, from the 84 TeV 1FHL sources, we reject 11 with the Sig_{30} cut, then 4 additional sources with the Γ_{10} cut and zero sources when applying the F_{50} cut. Therefore, VHE sources with low F_{50} also have low Sig_{30} and/or a low Γ_{10}. From the 15 TeV 1FHL sources that were rejected, we find that most of them (10 out of 15) are pulsars (6 HPSR and 4 PSR) that are associated with an extended PWN TeV source. Even though positional associations exist, the sources of the GeV radiation are not the sources of the TeV radiation. Among these 15 TeV 1FHL sources removed by the selection cuts are also the core of the Cen A radio galaxy, the FSRQ 3C 279, and VER J2016+372, a possible PWN. Cen A is an extremely weak TeV source whose detection required more than 120 hr of observation with H.E.S.S., and 3C 279 was detected by MAGIC only during two large outbursts in 2006 and 2007, but has not been detected during the Fermi LAT era. As for VER J2016+372, it is positionally coincident (angular separation is 0.°068) with the source 1FHL J2015.8+3710 (2FGL J2015.6+3709), which is associated with the FSRQ MG2 J201534+3710 ($z = 0.859$). However, the TeV source is probably associated with the PWN CTB 87, and not with the distant FSRQ (see Aliu 2011). The 2FGL source, which is mostly dominated by photons below 10 GeV, shows high variability and strong curvature in the spectrum, which is typical of bright, distant FSRQs. Above 10 GeV, the spectrum from 1FHL J2015.8+3710 seems to be somewhat harder ($\Gamma = 2.3 \pm 0.4$), which might suggest the presence of an additional component. But the spectral difference is not significant due to the low photon statistics and hence we cannot exclude a statistical fluctuation in the number of detected high-energy events.

Therefore, we do not consider the 13 LAT-detected sources discussed above (i.e., 10 pulsars plus Cen A, 3C 279, and MG2 J201534+3710/VER J2016+372) to be good candidates for detection with IACTs. The selection criteria remove

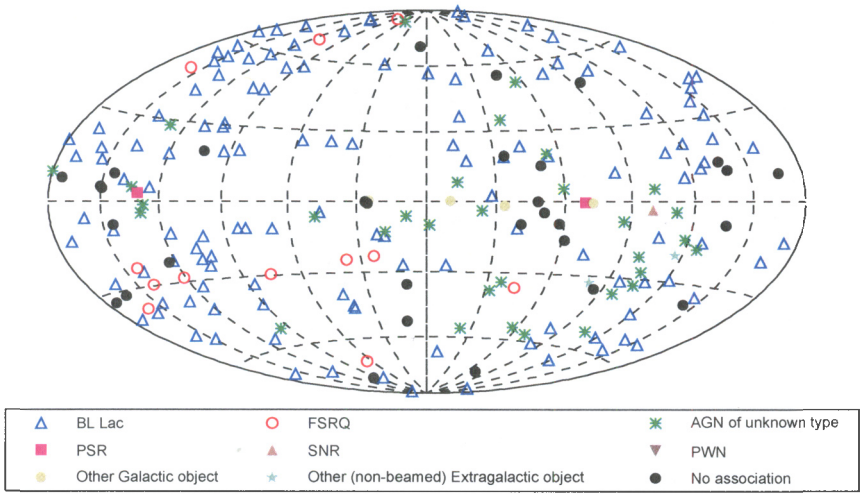

Figure 24. Sky map showing the 1FHL sources that we identify as good candidates for VHE detection. The markers represent the source classes in Table 4. The projection is Hammer–Aitoff in Galactic coordinates.

(A color version of this figure is available in the online journal.)

only two "good TeV candidate" sources: the blazar 1RXS J101015.9−311909, and the unidentified source HESS J1507−622. We conclude that the above-mentioned selection cuts are very conservative and that they keep most of the 1FHL sources that have already been detected at VHE.

5.2. Results from the Selection of TeV Candidates

From the 430 sources in the 1FHL catalog without VHE associations, we reject 175 with the cut on Sig_{30}, an additional 14 with the cut on Γ_{10} and finally 28 more with the cut on F_{50}. That is, the conservative selection criteria specified above remove about half of the 1FHL sources that have not yet been detected at VHE, and retain 212, among which are 128 with BL Lac associations, 12 with FSRQ associations, 32 AGUs, 2 PSRs, 3 SPP, 1 SNR (SNR G260.4−03.4), 1 LVB star (Eta Carinae), 1 radio galaxy (PKS 0625−35), 1 Galaxy (LMC), and 31 unassociated sources. These sources are denoted with the designator "C" in the column TEVCAT_FLAG in Table 3 and their locations are depicted in Figure 24.

Many of these 1FHL sources should be detectable with the current generation of ground-based γ-ray instruments. As this manuscript was being finalized, two of the sources in the TeV candidates list, associated with MS1221.8+2452 and H1722+119, were detected in the VHE band (Cortina 2013a, 2013b). These were naturally not included in the initial list of 84 1FHL sources that were detected at VHE, and so we have treated them as part of the 212-source VHE candidate list. The LAT detections above 10 GeV are already helping to substantially increase the number of VHE sources. For example, 1ES 1215+303 was detected by MAGIC in observations initiated based on an early version of this catalog (Mariotti 2011). The new generation of ground-based γ-ray observatories, namely HAWC, LHASSO and especially CTA, with lower energy thresholds and improved sensitivities, would have an even greater chance to detect a large fraction of the TeV candidates reported here.

6. POPULATION STUDIES

In the previous sections we reported results for γ-ray sources that are significantly detected with Fermi LAT at energies above 10 GeV in 3 yr of accumulated data. The probability for a γ-ray source to be detected at these high energies depends primarily on its γ-ray flux and its location with respect to the Galactic plane. As reported in Section 2.2, the PSF of the LAT is essentially independent of energy above 10 GeV, and the diffuse backgrounds are relatively dim (especially at high Galactic latitudes), and so the detection efficiency does not depend substantially on the spectral shapes of the sources. With the aid of Monte Carlo simulations, we can evaluate the detection efficiency of the instrument and from source population models infer the true numbers of sources above a given γ-ray flux below the detection limit and can infer the contribution of the resolved and unresolved sources to the diffuse backgrounds.

Given the substantial differences in the sensitivity of Fermi LAT for sources located at high/low Galactic latitudes (see Section 2.4), as well as the different natures of extragalactic and Galactic sources, and of the extragalactic (isotropic) and the Galactic (non-isotropic) diffuse backgrounds, we address this problem separately for extragalactic and Galactic sources in the following subsections.

6.1. Evaluation of the Extragalactic Source Count Distribution above 10 GeV

In this subsection we determine the source-count distribution (also known as N(S) or log N–log S) of the > 10 GeV extragalactic sky. Accurate knowledge of N(S) allows us to understand the contribution of sources to the isotropic γ-ray background (IGRB; Abdo et al. 2010o), constrain the

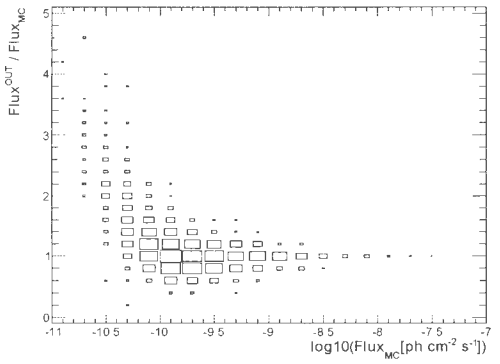

Figure 25. Ratio of measured to simulated flux vs. simulated flux (all above 10 GeV) for all sources with TS 25 and |b| 15°. For each cell the area of the box is proportional to the number of sources contained.

evolutionary properties of blazars (Ajello et al. 2012b), and predict the number of sources detectable by future γ-ray instruments.

We relate the observed flux distribution of sources to the intrinsic properties of the source population, such as N(S), by accounting for all of the observational biases that led to the detection of that particular source sample. Using the approach of Abdo et al. (2010p), we performed detailed Monte Carlo simulations in order to quantify these biases and correct for them. In short, we performed five end-to-end simulations of the LAT sky resembling as closely as possible the real observations. Each simulation was based on the real pointing history of the Fermi satellite during the time spanned by this analysis and comprises the Galactic and isotropic diffuse emissions and an isotropic source population.

The isotropic source population is modeled on the basis of properties of blazars determined in past Fermi observations. In particular, each source was modeled with a power-law spectrum in the 100 MeV–500 GeV band with flux and photon index randomly extracted from the distribution of N(S) and the power-law index distribution found by Abdo et al. (2010p). Each sky realization comprises >250,000 sources randomly distributed in the sky.

Photons of the P7CLEAN class in the whole 100 MeV–500 GeV band were generated using the P7CLEAN_V6 IRFs and the resulting simulated data were treated exactly as the real data. This means that only photons with measured energies >10 GeV and zenith angles <105° that were detected during times when the spacecraft rocking angle was less than 52° were retained. The source detection procedure was performed as for the real data (see Section 3.1) for all sources located at |b| 15°. We chose 15° Galactic latitude as a good compromise between maximizing source statistics and minimizing systematic errors in the reconstructed source flux due to the strong Galactic background (Abdo et al. 2010p). In each simulation ~500 sources were detected above 10 GeV with TS 25.

Figure 25 compares the reconstructed source fluxes ($Flux^{OUT}$) with the simulated ones ($Flux_{MC}$). At very low fluxes, the fluxes of the few detected sources in the simulation tend to be systematically overestimated. Due to the relatively low intensity of the diffuse background above 10 GeV, sources with fluxes of 10^{-10} photons cm^{-2} s^{-1} are significantly detected with ~10 photons. This number reduces to ~4 for the weakest detected sources. The large number of simulated sources (below the threshold) make it possible for a number of them to fluctuate above the threshold and be detected. This effect is often referred to as Eddington bias (Eddington 1913, 1940). The faintest source in the 1FHL catalog has a flux of 4.2×10^{-11} photons cm^{-2} s^{-1}, for which the bias is about 1.5. In any case, the efficiencies for source detection are evaluated as a function of measured (i.e., $Flux^{OUT}$) fluxes, hence automatically accounting for any bias.

Figure 26 shows the efficiency for detecting (simulated) sources as function of the reconstructed source flux. The detection efficiency is rather flat and about 100% above a flux of 10^{-10} photons cm^{-2} s^{-1}; a constant fit to the data points yields a detection efficiency of (98 ± 4)%. Below this flux, the detection efficiency decreases quickly, and at a flux of ~4×10^{-11} photons cm^{-2} s^{-1}, only 3 out of 100 (simulated) sources are detected.

The source count distribution can be derived as:

$$\frac{dN}{dS} = \frac{1}{\Delta S} \sum_{i=1}^{N_{\Delta S}} \frac{1}{\Omega_i} \quad (3)$$

where $N_{\Delta S}$ is the total number of detected sources with fluxes in the ΔS interval, and Ω_i is the solid angle associated with the flux of the i_{th} source (i.e., the detection efficiency multiplied by the survey solid angle). For the |b| 15° sample the geometric solid angle of the survey is 9.32 sr.

In order to parameterize the source count distribution we perform a maximum likelihood fit to the unbinned differential source counts using a simple power-law model: $dN/dS = A(S/10^{-7})^{-\beta}$. The best-fit parameters are $A = 20.6^{+6.7}_{-7.0}$ and $\beta = 2.19^{+0.06}_{-0.04}$ where the errors were computed via a bootstrap procedure (see Abdo et al. 2010p).

Figure 27 shows the differential distribution, with the power-law fit from the maximum-likelihood analysis (left), and the cumulative distribution (right). The cumulative distribution is also compared to the source counts derived by Abdo et al. (2010p) for the 10–100 GeV band, who used only 11 months of data. This comparison required converting the 10–100 GeV source counts to the 10–500 GeV band, which we did by adopting a power-law spectrum with a photon index of 2.5 (corresponding to a 3% increase of flux). It is apparent that the new N(S) extends to a factor ~1.8 lower fluxes due to the increased sensitivity.

As apparent from Figure 27, the source count distribution is compatible with a power law and does not show any significant flattening down to the lowest measured fluxes. This is in contrast to the N(S) of the full 100 MeV–100 GeV band (see Abdo et al. 2010p) and might have important consequences for the generation of the IGRB at these high energies (see below).

Since the detection efficiency does not depend on the source spectrum for energies >10 GeV (see Abdo et al. 2010p), the same efficiency curve can be used to derive the source-count distribution of FSRQs and BL Lac objects. Figure 28 shows the source counts for the FSRQ and BL Lac source populations. In the 10–500 GeV band and at the lowest fluxes measured by Fermi LAT, BL Lac objects are three times more numerous than FSRQs, reaching a density of ~0.01 BL Lac deg^{-2}. Therefore, the ratio of the source counts for BL Lac objects and FSRQs (an estimate of the "true" relative numbers) is similar to the ratio of the measured numbers of BL Lac objects and FSRQs (see Section 3.4). Since the spectral indices of FSRQs are typically about one unit softer than those of BL Lac objects

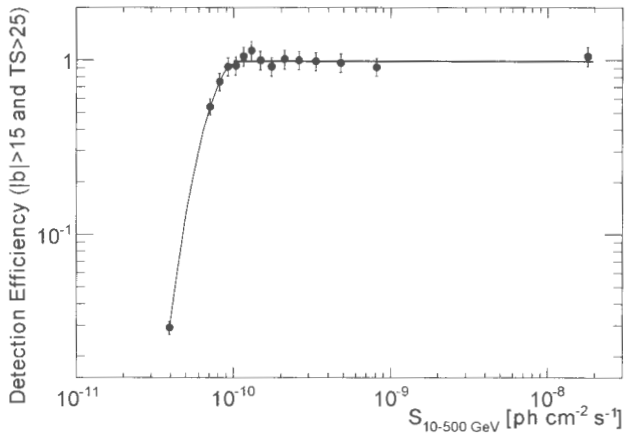

Figure 26. Detection efficiency as a function of measured flux for |b| 15° and TS 25. The error bars represent uncertainties from the counting statistic of our Monte Carlo simulations. The line above the flux 10^{-10} photons cm^{-2} s^{-1} results from a fit with a constant yielding 0.98 ± 0.04, while below this flux the curve smoothly connects the data points to guide the eye

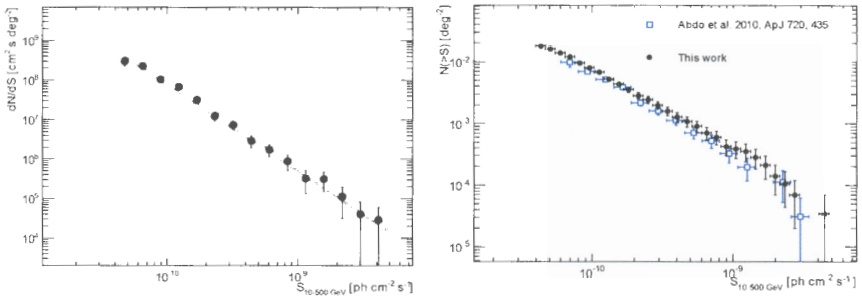

Figure 27. Left panel: differential N(S) (data points) and best-fit power-law model (gray line). Right panel: cumulative N(S) compared to the 10–100 GeV N(S) derived in Abdo et al. (2010p) using 11 months of data (converted to the 10–500 GeV band).

(A color version of this figure is available in the online journal.)

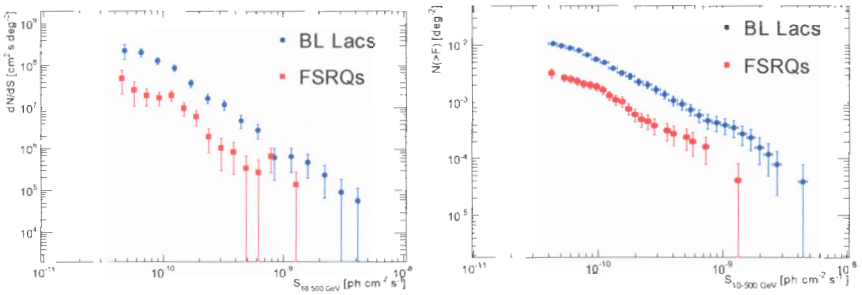

Figure 28. Differential N(S) (left panel) and cumulative N(S) (right panel) for BL Lac objects and FSRQs.

(A color version of this figure is available in the online journal.)

(see Figure 16), this result confirms that, above 10 GeV, the detection efficiency is not significantly affected by the different spectral shapes of the sources, as indicated above. Moreover, we also note that the N(S) of BL Lac objects does not flatten at the lowest measured fluxes while that of FSRQs seems to flatten below ~ 10^{-10} photons cm^{-2} s^{-1}.

From the source flux distribution we can determine how much of the intensity of the IGRB above 10 GeV is due to 1FHL

sources. The comparison between the N(S) derived here and the IGRB measurement reported by Abdo et al. (2010o) is not straightforward. Indeed, the two works rely on sources detected on different timescales and above different thresholds. Sources used by Abdo et al. (2010o) were detected with TS 25 in the 0.2–100 GeV band using nine months of data while those used here are detected with TS 25 in the 10 500 GeV band using 3 yr of data.

The most straightforward comparison is between the total sky intensities, by which we mean the intensity of the IGRB plus the detected sources. From fitting band-by-band intensities of the IGRB reported in Table 1 of Abdo et al. (2010o) with a power-law function above 10 GeV, and integrating the fitted function in the energy range 10–500 GeV, one can find that the intensity of the IGRB in the 10-500 GeV band is $(1.5 \pm 0.3) \times 10^{-8}$ photons cm^{-2} s^{-1} sr^{-1}. The resolved sources account for a further $(0.8 \pm 0.1) \times 10^{-8}$ photons cm^{-2} s^{-1} sr^{-1}, and the total isotropic intensity in the 10–500 GeV band is $(2.3 \pm 0.3) \times 10^{-8}$ photons cm^{-2} s^{-1} sr^{-1}.

The diffuse flux produced by an unresolved source population can be obtained as:

$$S_{\rm diffuse} = \int_{S_{\rm min}}^{S_{\rm max}} dS \frac{dN}{dS} S \quad 1 - \frac{\Omega(S)}{\Omega_{\rm max}} \qquad (4)$$

where $\Omega_{\rm max}$ is the geometrical sky area and the $\Omega(S)/\Omega_{\rm max}$ term (which is the detection efficiency reported in Figure 26) takes into account the dependency of the LAT source detection efficiency on the source flux.

Setting $\Omega(S)/\Omega_{\rm max} = 0$ allows us to evaluate the total diffuse flux including resolved sources. Integrating the N(S) to the minimum observed flux of 4.2×10^{-11} photons cm^{-2} s^{-1} we obtain $S_{\rm total} = (10.6 \pm 1.0) \times 10^{-9}$ photons cm^{-2} s^{-1} sr^{-1}, where the error was computed through a bootstrap procedure, following Abdo et al. (2010p). This shows that 1FHL sources account for about half of the total (IGRB plus sources) sky intensity in the energy band 10–500 GeV.

Most of the comparisons presented in the literature refer to the diffuse emission arising from unresolved sources. Using Equation (4), the flux from the unresolved sources can be computed to be $3.9^{+0.8}_{-0.6} \times 10^{-9}$ photons cm^{-2} s^{-1} sr^{-1}, where the uncertainty is primarily due the statistical and systematic uncertainties of the detection efficiency, and the contribution from the statistical *uncer*tainty of the bootstrap procedure is minor (Abdo et al. 2010p).

As a consistency check, one can compare the resolved source flux determined in different ways. The true flux of sources detected in this work, which can be obtained by averaging the fluxes of all the |b| 15° detected sources, amounts to $(8.2 \pm 0.1) \times 10^{-9}$ photons cm^{-2} s^{-1} sr^{-1}, and *is com*patible with the number derived from Abdo et al. (2010o) that was reported above. Additionally, one can also derive the source flux by subtracting from the total diffuse flux ($(10.6 \pm 1.0) \times 10^{-9}$ photons cm^{-2} s^{-1} sr^{-1}) the unresolved source flux ($3.9 \pm 0.8 \times 10^{-9}$ photons cm^{-2} s^{-1} sr^{-1}), obtaining $(6.7 \pm 1.3) \times 10^{-9}$ photons cm^{-2} s^{-1} sr^{-1}, which is comparable to the above-mentioned estimates.

In conclusion, unresolved 1FHL sources with S 4×10^{-11} photons cm^{-2} s^{-1} sr^{-1} account for $3.9^{+0.8}_{-0.6} \times 10^{-9}$ photons cm^{-2} s^{-1} sr^{-1}, which is $27 \pm 8\%$ of the IGRB emission above 10 GeV reported in Abdo et al. (2010o). We note that this contribution to the IGRB is substantially larger than the 9% lower limit reported by Abdo et al (2010p) and is, in large part, due to the increased sensitivity (the N(S) samples a factor ~2 weaker fluxes), and also to a better treatment of the resolved source flux. It is reasonable to expect that 1FHL sources produce an even larger fraction of the diffuse emission than found in the earlier work since Equation (4) has been integrated only to the lowest flux observed, and the N(S) does not yet show any strong flattening.

6.2. Galactic Sources

Here we analyze the population of Galactic sources to estimate the contribution of unresolved sources to the Galactic "diffuse" emission, following the method of Strong (2007). We adopt a plausible reference model for the space density and luminosity function of Galactic sources and investigate the sensitivity of the results to the assumptions of the model.

The luminosity function at Galactocentric distance R and distance from Galactic plane z is the space density of sources per unit luminosity $\rho(L_\gamma, R, z)$. After Strong (2007) we assume that the luminosity function depends on luminosity as L_γ^{-u} for $L_{\gamma,\rm min} < L_\gamma < L_{\gamma,\rm max}$ and is zero outside these limits. The total space density of sources is $\rho(R, z) = \int \rho(L_\gamma, R, z)\, dL_\gamma$, which we normalize to the value ρ at $(R, z) = (R\ , 0)$. For a source of luminosity L_γ at distance d the flux is $S_\gamma = L_\gamma / 4\pi d^2$. The differential source counts are defined as $N(S_\gamma)$ sources per unit flux over the area of sky considered. At lower S_γ, both the luminosity function and the spatial boundaries influence $N(S_\gamma)$. In practice the sources are binned in $\log(S_\gamma)$ so that plotted distributions are proportional to $S_\gamma N(S_\gamma)$.

For S_γ large enough that the spatial boundaries of the distribution have no influence on the detectability, the well-known relations $N(S_\gamma) \propto S_\gamma^{-5/2}$, S_γ^{-2} hold for three-dimensional and two-dimensional spatial source distributions, respectively, independent of the shape of the luminosity function.[101] These apply to low luminosity/ high space density (quasi-isotropic) and high luminosity/ low space density (Galactic plane) populations respectively.

As in Strong (2007) we use standard Monte Carlo techniques to sample $\rho(L_\gamma, R, z)$ throughout the Galaxy, using oversampling to reduce statistical fluctuations if necessary. In these simulations we did not vary the source spectra because we did not consider spectral information in source detection, only the flux > 10 GeV. We use the sources generated from such simulations to form simulated catalogs extending below the 1FHL flux limit and compare the flux distributions with the observations.

Our reference model for the luminosity function has ρ = 3 kpc^{-3}, and $L_\gamma^{-1.5}$ dependence on luminosity in the range 10^{34} 10^{37} photons s^{-1} above 10 GeV. The luminosity law is discussed in Strong (2007); the exact form is not critical and will not be further addressed here. The distribution in Galactocentric distance is based on the model of Lorimer et al. (2006) for the distribution of pulsars, taken as representative of Galactic sources. We adopt an exponential scale height of 500 pc; the source count distribution $N(S_\gamma)$ depends only weakly on the

[101] Standard proof for uniform space density: for number n(< R) within distance R with luminosity L, $S \propto L/R^2$, $N(S) = dn/dS = dn/dR \times dR/dS = S^{-3/2} dn/dR$; three-dimensional volume: $n \propto R^3$, $dn/dR \propto R^2 \propto S^{-1} \rightarrow N(S) \propto S^{-5/2}$; two-dimensional disk: $n \propto R^2$, $dn/dR \propto R \propto S^{-1/2} \rightarrow N(S) \propto S^{-2}$. Integrating over a luminosity function $\rho(L)$ does not affect the dependence on S, hence the shape is independent of $\rho(L)$. This is valid when boundaries do not influence N(S). At lower S_γ, both the luminosity function and the spatial boundaries influence $N(S_\gamma)$. For a boundary at $R_{\rm max}$, there will be a cutoff in N(S) below $S = L_{\rm min}/4\pi R_{\rm max}^2$, where $L_{\rm min}$ is the minimum luminosity contributing to $\rho(L)$.

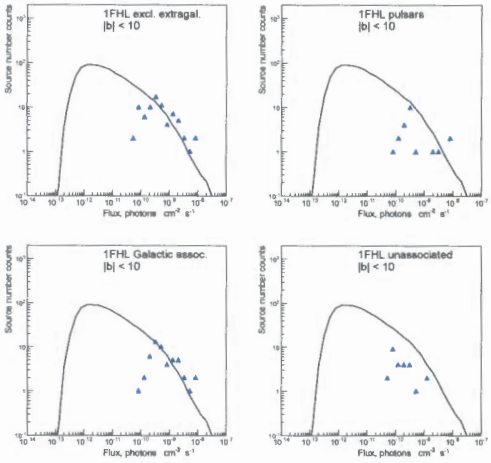

Figure 29. Low-latitude ($|b| < 10^{\circ}$) source number counts for Galactic and unassociated sources above 10 GeV compared with the reference model described in the text. The blue triangles are source counts from the 1FHL catalog; Top left: all 1FHL sources, excluding those associated with extragalactic sources, right: 1FHL pulsars, Bottom left: all 1FHL sources with Galactic associations (including pulsars), right: unassociated sources.

(A color version of this figure is available in the online journal.)

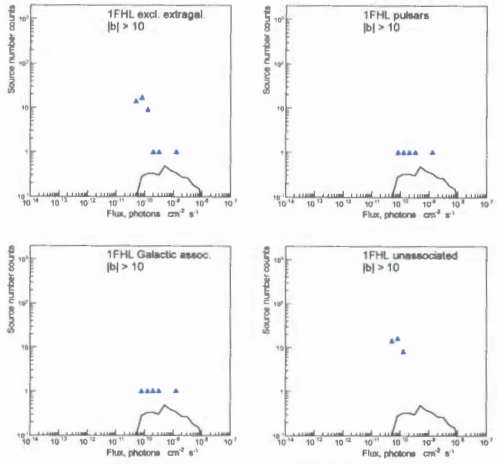

Figure 30. High-latitude ($|b| > 10^{\circ}$) source number counts for Galactic and unassociated sources above 10 GeV compared with the reference model described in the text. The blue triangles are source counts from the 1FHL sources; Top left: all 1FHL sources, excluding those associated with extragalactic sources, right: 1FHL pulsars, Bottom left: all 1FHL sources with Galactic associations (including pulsars), right: unassociated sources.

(A color version of this figure is available in the online journal.)

scale height. This distribution peaks near R = 4 kpc and falls to zero at R = 0; it was chosen for illustration and has not been optimized for the 1FHL source counts.

Figures 29 and 30 compare the simulated $N(S_\gamma)$ with the observed flux distributions of 1FHL sources at low latitudes ($|b| < 10^{\circ}$) and high latitudes ($|b| > 10^{\circ}$), respectively. The unassociated sources at low latitudes are a mixture of Galactic and AGN sources, although the proportion is unknown. The pure Galactic, and the combined Galactic and unassociated sample, can therefore be used to test the models. The reference model is consistent with the low-latitude source counts, having the observed dependence on flux above the source detection threshold; the slope reflects the spatial distribution (independent of the shape of the luminosity function) above 10^{-9} photons $cm^{-2}\,s^{-1}$, while the distributions for both the model and observed source counts flatten at lower fluxes.

Figure 29 shows that the distribution of simulated sources (in the reference model) continues down to fluxes ~ 100 times below the detection threshold, the cutoff being due to the finite spatial extent of the Galaxy. The ratio of total flux below threshold to above threshold is 0.3, which gives an estimate of the contribution of the undetected sources to the "diffuse" emission (see below).

Figure 29 also presents the source count distributions for identified and associated Galactic sources only, indicating a reduction of low-flux sources relative to the counts distributions that also include unassociated sources. Pulsars are also shown separately; they account for about half of these sources, and this shows how their contribution compares with the unassociated ones. The similarity of the observed $N(S_\gamma)$ for the total (non-blazar) and unassociated sources is consistent with their being similar populations.

In Figure 30 the reference model is seen to be consistent with the high-latitude $N(S_\gamma)$, since it lies below the observed source counts (which contain unidentified AGNs). The identified high-latitude Galactic sources (all pulsars) are under-predicted by a factor 3 (but there are only 5 sources in the sample). A higher density of Galactic sources would improve the agreement, and retain consistency with the low-latitude counts if the luminosities are correspondingly decreased, for example with $\rho_{\odot} = 10$ kpc^{-3} and 4×10^{33}–4×10^{36} photons s^{-1}. This case is shown in Figure 31 (upper row). This model fits the Galactic sources at both low and high latitudes and is therefore another possible combination of parameters consistent with the data. Large deviations from these values are excluded by the combination of low and high-latitude $N(S_\gamma)$. We note that the full quoted luminosity range is required, the low end by high-latitude nearby low-luminosity sources, the high end by low-latitude distant high-luminosity sources. Therefore the contribution to the unresolved emission from sources below threshold at low latitudes in Figures 29 and 31 is a necessary consequence of the observed $N(S_\gamma)$.

Although most high-latitude unassociated sources are probably AGNs, a fraction may be pulsars or other objects, implying a greater density of Galactic sources. To illustrate this, we increase the source density so that 30% of the unassociated high-latitude sources are Galactic sources (Figure 31, lower row); to satisfy the low-latitude $N(S_\gamma)$ the luminosity range has to be decreased to 1.5×10^{33}–1.5×10^{36} ph s^{-1}. In this case the contribution to the unresolved emission from sources below threshold at low latitudes is larger (see below).

Using the reference model, we evaluate the contribution to the observed γ-ray intensity (> 10 GeV) at low latitudes ($|b| < 10^{\circ}$, all longitudes). Here we adopt a detection threshold of 5×10^{-10} photons $cm^{-2}\,s^{-1}$ (Section 2.4). For the reference model shown in Figures 29 and 30, 20% of the emission is contributed by sources below the threshold. The total flux is 7×10^{-8} and 2×10^{-8} photons $cm^{-2}\,s^{-1}$ from above and below

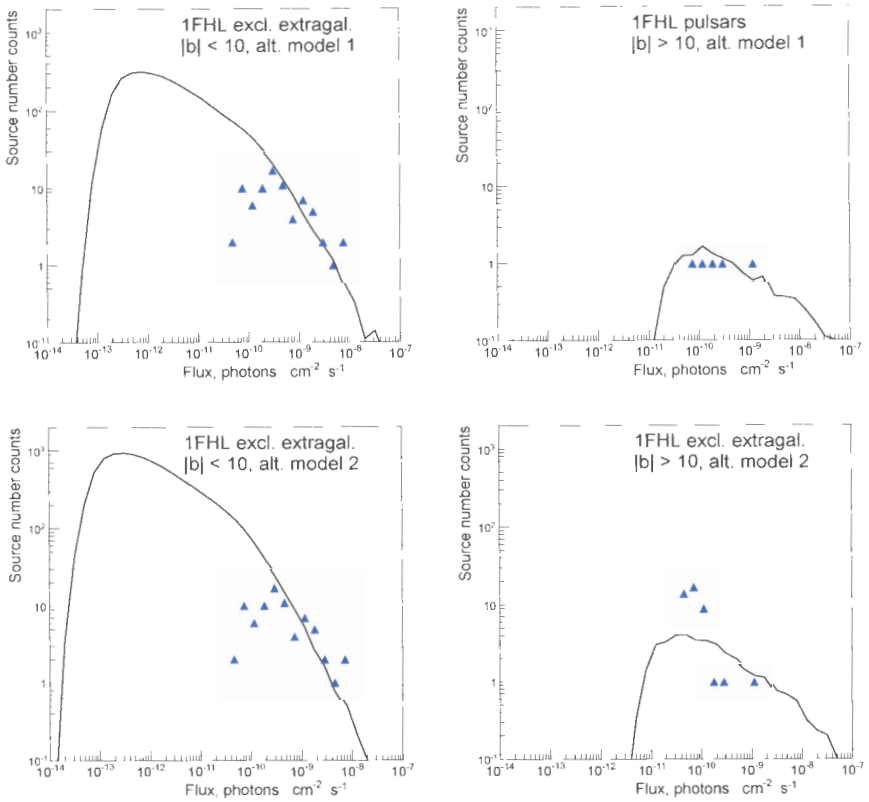

Figure 31. Source number counts for sources above 10 GeV at low and high latitudes, compared with modified models for the luminosity function. For the upper row the local source density has been increased to $\rho = 10$ kpc^{-3}, and γ-ray luminosity range decreased to 4×10^{33}–4×10^{36} photons s^{-1} above 10 GeV (labeled as alternative model 1). For the lower row $\rho = 30$ kpc^{-3} and the luminosity range is 1.5×10^{33}–1.5×10^{36} photons s^{-1}, for the same γ-ray luminosity law $L_\gamma^{-1.5}$ and spatial distribution as the reference model (labeled as alternative model 2). The blue triangles are derived from the 1FHL data: Upper left: $|b| < 10°$, all 1FHL sources, excluding those associated with extragalactic sources, right: $|b| > 10°$, 1FHL pulsars, Lower left: $|b| < 10°$, all 1FHL sources, excluding those associated with extragalactic sources, right: $|b| > 10°$, all 1FHL sources, excluding those associated with extragalactic sources.

(A color version of this figure is available in the online journal.)

this threshold, respectively. The total "diffuse" flux observed by Fermi-LAT from this region is $\sim 8 \times 10^{-7}$ photons cm^{-2} s^{-1} (Ackermann et al. 2012a). Hence about 2.5% of the Galactic "diffuse" emission is from undetected sources. For the "higher density" model shown in Figure 31 (upper row), 30% of the emission is contributed by sources below the threshold, increasing to ~4% the fraction of "diffuse" emission from undetected sources. For the "maximum density" model shown in Figure 31 (lower row), 50% of the emission is contributed by sources below the threshold, and the contribution of unresolved sources to the overall Galactic "diffuse" emission is ~ 8%. These results are similar to previous estimates at lower energies (Strong 2007), but this is the first time a value for > 10 GeV has been derived.

A similar approach to using source counts to constrain the pulsar contribution to the inner Galaxy emission has been given by Hooper et al. (2013), concluding that pulsars cannot account for the GeV excess. A study of the MSP contribution to the Galactic emission, for energies above 100 MeV, has been given by Grégoire & Knödlseder (2011, 2013); the contribution is at the few percent level.

Finally we consider the global picture. The total luminosity of the source population > 10 GeV based on the reference model is 2.6×10^{38} photons s^{-1} or about 4×10^{36} erg s^{-1} compared to the total luminosity of the Galaxy from interstellar emission in this range: 3×10^{39} photons s^{-1} or 5×10^{37} erg s^{-1} (Strong et al. 2010). Point sources, resolved or not, therefore contribute at the several percent level to the total luminosity of the Galaxy, with a correspondingly larger contribution for the higher-density models.

7. DISCUSSION AND CONCLUSIONS

The first Fermi LAT catalog of sources above 10 GeV is a catalog of the highest-energy LAT sources. With its focus on high-energy data, the 1FHL explores how the γ-ray

universe evolves between the 2FGL catalog (which is dominated by emission between 100 MeV and 10 GeV) and the VHE sources detected with ground-based γ-ray instruments (which are dominated by emission from 100 GeV and up).

The 1FHL catalog contains 514 sources. Because of the steepness of the source count distribution N(S), and the relatively low intensity of diffuse backgrounds (Galactic, extragalactic isotropic, and residual cosmic rays) at > 10 GeV, which make source detection (TS > 25) possible with only a few γ-rays, a large number of the > 10 GeV sources are detected close to the threshold, and the median number of γ rays per source is 13. This very low photon count limits the possibilities for detailed spectral and variability analyses. We have provided only power-law spectral fits, and applied the Bayesian Block (Scargle 1998) algorithm to study variability without pre-defined temporal bins. Our analysis treated 22 sources as spatially extended, because they have been resolved in previous LAT analyses, typically at lower energies. For these sources, we adopted their extents as measured in the previous works.

We studied potential associations between 1FHL sources and counterparts at other wavelengths. Approximately 75% have likely associations with AGNs. Galactic sources (pulsars, PWNs, SNRs, high-mass binaries, and star-forming regions) collectively represent 10% of the sources. The fraction of unassociated sources is only 13%. Among the 27 associations with known pulsars, we find 20 with significant pulsations above 10 GeV, and 12 with pulsations above 25 GeV, suggesting that the Crab pulsar will not remain the only pulsar to be detected by current and future IACTs.

We detected variability for 43 1FHL sources, all belonging to the blazar class. We found that the most variable of these belong to the SED class LSP, which in some cases have very bright (10×) and very short (~1 day) flaring episodes. This result is remarkable because HSP sources (rather than LSP) typically have the largest numbers of detected γ-rays above 10 GeV. The implication is that the falling segment of the high-energy (presumably inverse-Compton) bump is more variable than the rising segment. This result is consistent with the trend reported at lower energies (> 100 MeV) by Ackermann et al (2011b).

Based on the 84 associations between 1FHL sources and known VHE sources, we developed criteria to select other sources that are likely to be detectable with ground-based γ-ray instruments. Of the 1FHL sources not already detected in the VHE range, we flagged 212 as good candidates based on their average properties for the 3 yr time range of the analysis.

Using the source counts for blazars we estimate that 27% ± 8% of the IGRB for energies > 10 GeV can be attributed to blazars. This contribution to the IGRB in the range > 10 GeV is well above the lower limit of Abdo et al. (2010p); the measurement was enabled by the greater sensitivity here: the 3 yr N(S) samples a factor ~2 weaker fluxes than the 11-month N(S). Since the N(S) does not show any flattening at the lowest measured fluxes, the contribution from blazars may be even larger. Fermi might survey the sky for 10 yr or more, potentially providing a further improvement in the > 10 GeV sensitivity of the same magnitude (a factor ~2) as that provided in this work with respect to the 11 months of survey data analyzed by Abdo et al. (2010p). Fermi LAT ultimately could be able to directly resolve > 40% of the IGRB intensity above 10 GeV.

The source count distributions for sources in the Milky Way (i.e., those with associations with Galactic source classes) and more generally for sources without extragalactic associations, can be well modeled with a power-law luminosity function for sources with characteristic luminosities in the range 10^{34}–10^{37} ph s^{-1} above 10 GeV and a distribution in Galactocentric distance based on the pulsar distribution of Lorimer et al. (2006) and a scale height of 500 pc. From the models, we estimate that ~5% of the luminosity of the Milky Way above 10 GeV can be attributed to unresolved γ-ray point sources.

The Fermi LAT Collaboration acknowledges generous ongoing support from a number of agencies and institutes that have supported both the development and the operation of the LAT as well as scientific data analysis. These include the National Aeronautics and Space Administration and the Department of Energy in the United States; the Commissariat à l'Energie Atomique and the Centre National de la Recherche Scientifique/ Institut National de Physique Nucléaire et de Physique des Particules in France; the Agenzia Spaziale Italiana and the Istituto Nazionale di Fisica Nucleare in Italy; the Ministry of Education, Culture, Sports, Science, and Technology (MEXT), High Energy Accelerator Research Organization (KEK), and Japan Aerospace Exploration Agency (JAXA) in Japan; and the K. A. Wallenberg Foundation, the Swedish Research Council, and the Swedish National Space Board in Sweden.

Additional support for science analysis during the operations phase is gratefully acknowledged from the Istituto Nazionale di Astrofisica in Italy and the Centre National d'Études Spatiales in France.

M. Ajello acknowledges support from NASA grant NNH09ZDA001N for the study of the origin of the Isotropic Gamma-ray Background. D. Paneque acknowledges support from NASA grant NNX10AP21G for the study of the highest-energy LAT sources.

Facility: Fermi (LAT)

REFERENCES

Abdo, A. A., Ackermann, M., Agudo, I., et al. 2010a, ApJ, 716, 30
Abdo, A. A., Ackermann, M., Ajello, M., et al. 2009a, Sci, 325, 848
Abdo, A. A., Ackermann, M., Ajello, M., et al. 2009b, Sci, 325, 840
Abdo, A. A., Ackermann, M., Ajello, M., et al. 2009c, ApJL, 699, L102
Abdo, A. A., Ackermann, M., Ajello, M., et al. 2009d, ApJ, 706, 1331
Abdo, A. A., Ackermann, M., Ajello, M., et al. 2009e, ApJL, 706, L1
Abdo, A. A., Ackermann, M., Ajello, M., et al. 2009f, ApJ, 700, 1059
Abdo, A. A., Ackermann, M., Ajello, M., et al. 2010b, ApJ, 714, 927
Abdo, A. A., Ackermann, M., Ajello, M., et al. 2010c, A&A, 523, A46
Abdo, A. A., Ackermann, M., Ajello, M., et al. 2010d, Sci, 328, 725
Abdo, A. A., Ackermann, M., Ajello, M., et al. 2010e, ApJS, 188, 405
Abdo, A. A., Ackermann, M., Ajello, M., et al. 2010f, ApJ, 712, 1209
Abdo, A. A., Ackermann, M., Ajello, M., et al. 2010g, ApJ, 708, 1254
Abdo, A. A., Ackermann, M., Ajello, M., et al. 2010h, ApJ, 718, 348
Abdo, A. A., Ackermann, M., Ajello, M., et al. 2010i, ApJ, 713, 146
Abdo, A. A., Ackermann, M., Ajello, M., et al. 2010j, ApJ, 720, 272
Abdo, A. A., Ackermann, M., Ajello, M., et al. 2010k, Sci, 327, 1103
Abdo, A. A., Ackermann, M., Ajello, M., et al. 2010l, ApJ, 712, 459
Abdo, A. A., Ackermann, M., Ajello, M., et al. 2010m, A&A, 512, A7
Abdo, A. A., Ackermann, M., Ajello, M., et al. 2010n, ApJ, 711, 64
Abdo, A. A., Ackermann, M., Ajello, M., et al. 2010o, PRL, 104, 101101
Abdo, A. A., Ackermann, M., Ajello, M., et al. 2010p, ApJ, 720, 435
Abdo, A. A., Ackermann, M., Ajello, M., et al. 2010q, ApJ, 713, 154
Abdo, A. A., Ackermann, M., Ajello, M., et al. 2011a, ApJL, 733, L26
Abdo, A. A., Ackermann, M., Ajello, M., et al. 2011b, ApJ, 726, 43
Abdo, A. A., Ackermann, M., Ajello, M., et al. 2011c, ApJ, 734, 28
Abdo, A. A., Ackermann, M., Atwood, W. B., et al. 2008, Sci, 322, 1218
Abdo, A. A., Ackermann, M., Atwood, W. B., et al. 2009g, ApJL, 695, L72
Abdo, A. A., Ackermann, M., Atwood, W. B., et al. 2009h, ApJ, 696, 1084
Abdo, A. A., Ajello, M., Allafort, A., et al. 2013, ApJS, 208, 17
Abdo, A. A., Ajello, M., Antolini, E., et al. 2010r, ApJ, 720, 26
Abdo, A. A., Allen, B. T., Aune, T., et al. 2009i, ApJL, 700, L127
Abramowski, A., Acero, F., Aharonian, F., et al. 2012, ApJ, 746, 151

Acciari, V. A., Aliu, E., Arlen, T., et al. 2009, ApJL, 703, L6
Acero, F., Ackermann, M., Ajello, M., et al. 2013, ApJ, 773, 77
Ackermann, M., Ajello, M., Allafort, A., et al. 2011a, Sci, 334, 1103
Ackermann, M., Ajello, M., Allafort, A., et al. 2011b, ApJ, 743, 171
Ackermann, M., Ajello, M., Atwood, W. B., et al. 2012a, ApJ, 750, 3
Ackermann, M., Ajello, M., Albert, A., et al. 2012b, ApJS, 203, 4
Ackermann, M., Ajello, M., Baldini, L., et al. 2010, ApJ, 721, 1383
Ackermann, M., Ajello, M., Baldini, L., et al. 2011c, ApJ, 726, 35
Aharonian, F., Akhperjanian, A. G., Anton, G., et al. 2009, ApJL, 695, L40
Ajello, M., Allafort, A., Baldini, L., et al. 2012a, ApJ, 744, 80
Ajello, M., Shaw, M. S., Romani, R. W., et al. 2012b, ApJ, 751, 108
Aleksić, J., Alvarez, E. A., Antonelli, L. A., et al. 2012a, A&A, 539, L2
Aleksić, J., Alvarez, E. A., Antonelli, L. A., et al. 2012b, A&A, 540, A69
Aleksić, J., Antonelli, L. A., Antoranz, P., et al. 2010, ApJ, 725, 1629
Aleksić, J., Antonelli, L. A., Antoranz, P., et al. 2011, ApJL, 730, L8
Aliu, E. 2011, in ICRC, 7, 227
Aliu, E., Anderhub, H., Antonelli, L. A., et al. 2008, Sci, 322, 1221
Aliu, E., Archambault, S., Arlen, T., et al. 2013, ApJ, 764, 38
Atkins, R., Benbow, W., Berley, D., et al. 2004, ApJ, 608, 680
Atwood, W. B., Abdo, A. A., Ackermann, M., et al. 2009, ApJ, 697, 1071
Bernlöhr, K., Barnacka, A., Becherini, Y., et al. 2013, APh, 43, 171
Bulgarelli, A., Gianotti, F., Trifoglio, M., et al. 2010, ATel, 2641, 1
Camilo, F., Ray, P. S., Ransom, S. M., et al. 2009, ApJ, 705, 1
Campana, R., Massaro, E., Gasparrini, D., Cutini, S., & Tramacere, A. 2008, MNRAS, 383, 1166
Casandjian, J.-M., & Grenier, I. A. 2008, A&A, 489, 849
Ciprini, S., Tosti, G., Marcucci, F., et al. 2007, in AIP Conf. Ser. 921, The First GLAST Symposium, ed. S. Ritz, P. Michelson, & C. A. Meegan (Melville, NY: AIP), 546
Cognard, I., Guillemot, L., Johnson, T. J., et al. 2011, ApJ, 732, 47
Condon, J. J., Cotton, W. D., Greisen, E. W., et al. 1998, AJ, 115, 1693
Cortina, J. 2013a, ATel, 5080, 1
Cortina, J. 2013b, ATel, 5038, 1
Damiani, F., Maggio, A., Micela, G., & Sciortino, S. 1997, ApJ, 483, 350
de Jager, O. C., Raubenheimer, B. C., & Swanepoel, J. W. H. 1989, A&A, 221, 180
de Ruiter, H. R., Arp, H. C., & Willis, A. G. 1977, A&AS, 28, 211
Donato, D. 2010, ATel, 2584, 1
Eddington, A. S. 1913, MNRAS, 73, 359
Eddington, A. S., Sir 1940, MNRAS, 100, 354
Galante, N. 2011, in ICRC, 8, 62
Grégoire, T., & Knödlseder, J. 2011, in AIP Conf. Proc. 1357, Radio Pulsars: an Astrophysical Key to Unlock the Secrets of the Universe, ed. M. Burgay, N. D'Amico, P. Esposito, A. Pellizzoni, & A. Possenti (Melville, NY: AIP), 197
Grégoire, T., & Knödlseder, J. 2013, A&A, 554, A62
Grondin, M.-H., Funk, S., Lemoine-Goumard, M., et al. 2011, ApJ, 738, 42
Guillemot, L., Freire, P. C. C., Cognard, I., et al. 2012, MNRAS, 422, 1294
Hadasch, D., Torres, D. F., Tanaka, T., et al. 2012, ApJ, 749, 54
Halpern, J. P., Camilo, F., Giuliani, A., et al. 2008, ApJL, 688, L33
Hartman, R. C., Bertsch, D. L., Bloom, S. D., et al. 1999, ApJS, 123, 79
Helene, O. 1983, NIMPR, 212, 319
Hinton, J. A. 2004, NewAR, 48, 331
Hooper, D., Cholis, I., Linden, T., Siegal-Gaskins, J., & Slatyer, T. 2013, PhRvD, 88, 083009
Iafrate, G., Longo, F., & D'Ammando, F. 2010, ATel, 2687, 1
Jackson, B., Scargle, J. D., Barnes, D., et al. 2005, ISPL, 12, 105
Kadler, M., Eisenacher, D., Ros, E., et al. 2012, A&A, 538, L1
Katagiri, H., Tibaldo, L., Ballet, J., et al. 2011, ApJ, 741, 44
Kataoka, J., Stawarz, L., Cheung, C. C., et al. 2010, ApJ, 715, 554
Katsuta, J., Uchiyama, Y., Tanaka, T., et al. 2012, ApJ, 752, 135
Kerr, M. 2010, PhD thesis, Univ. Washington
Kerr, M., Camilo, F., Johnson, T. J., et al. 2012, ApJL, 748, L2
Klepser, S. 2011, in ICRC, 7, 172
Lamb, R. C., & Macomb, D. J. 1997, ApJ, 488, 872
Lande, J., Ackermann, M., Allafort, A., et al. 2012, ApJ, 756, 5
Lorenz, E. 2004, NewAR, 48, 339
Lorimer, D. R., Faulkner, A. J., Lyne, A. G., et al. 2006, MNRAS, 372, 777
Mariotti, M. 2010, ATel, 2684, 1
Mariotti, M. 2011, ATel, 3100, 1
Massardi, M., Ekers, R. D., Murphy, T., et al. 2011, MNRAS, 412, 318
Massaro, E., Giommi, P., Leto, C., et al. 2009, A&A, 495, 691
Mauch, T., Murphy, T., Buttery, H. J., et al. 2003, MNRAS, 342, 1117
Murphy, T., Sadler, E. M., Ekers, R. D., et al. 2010, MNRAS, 402, 2403
Neronov, A., & Semikoz, D. V. 2010, arXiv:1011.0210
Neronov, A., Semikoz, D., & Vovk, I. 2011, A&A, 529, A59
Nolan, P. L., Abdo, A. A., Ackermann, M., et al. 2012, ApJS, 199, 31
Ong, R. A. 2010, ATel, 2443, 1
Planck Collaboration, Ade, P. A. R., Aghanim, N., et al. 2011, A&A, 536, A7
Pletsch, H. J., Guillemot, L., Allen, B., et al. 2012a, ApJ, 744, 105
Pletsch, H. J., Guillemot, L., Allen, B., et al. 2012b, ApJL, 755, L20
Ransom, S. M., Ray, P. S., Camilo, F., et al. 2011, ApJL, 727, L16
Sanchez, D., & Escande, L. 2010, ATel, 3041, 1
Saz Parkinson, P. M., Dormody, M., Ziegler, M., et al. 2010, ApJ, 725, 571
Scargle, J. D. 1998, ApJ, 504, 405
Scargle, J. D., Norris, J. P., Jackson, B., & Chiang, J. 2013, ApJ, 764, 167
Shaw, M. S., Romani, R. W., Cotter, G., et al. 2013, ApJ, 764, 135
Sokolovksy, K. V., Schinzel, F. K., Tanaka, Y. T., et al. 2013, A&A, submitted
Starck, J.-L., & Pierre, M. 1998, A&AS, 128, 397
Striani, E., Vercellone, S., Lucarelli, F., et al. 2010a, ATel, 3043, 1
Striani, E., Verrecchia, F., Donnarumma, I., et al. 2010b, ATel, 2686, 1
Strong, A. W. 2007, Ap&SS, 309, 35
Strong, A. W., Porter, T. A., Digel, S. W., et al. 2010, ApJL, 722, L58
Su, M., Slatyer, T. R., & Finkbeiner, D. P. 2010, ApJ, 724, 1044
Sun, S., Paneque, D., Steinke, B., Galante, N., & Fortson, L. 2012, in 5th International Symposium on High-Energy Gamma-Ray Astronomy
Sutherland, W., & Saunders, W. 1992, MNRAS, 259, 413
Swordy, S. 2008, ATel, 1753, 1
Tanaka, T., Allafort, A., Ballet, J., et al. 2011, ApJL, 740, L51
The MAGIC Collaboration, Aleksić, J., Antonelli, L. A., et al. 2013, arXiv:1305.5147
Thompson, D. J., Bertsch, D. L., & O'Neal, R. H., Jr. 2005, ApJS, 157, 324
VERITAS Collaboration, Aliu, E., Arlen, T., et al. 2011, Sci, 334, 69
Véron-Cetty, M.-P., & Véron, P. 2010, A&A, 518, A10
Voges, W., Aschenbach, B., Boller, T., et al. 1999, A&A, 349, 389
Weekes, T. C., Badran, H., Biller, S. D., et al. 2002, APh, 17, 221
Weltevrede, P., Abdo, A. A., Ackermann, M., et al. 2010, ApJ, 708, 1426
Wills, K. A., Morganti, R., Tadhunter, C. N., Robinson, T. G., & Villar-Martin, M. 2004, MNRAS, 347, 771
Wright, A. E., Griffith, M. R., Hunt, A. J., et al. 1996, ApJS, 103, 145